Summary Data from the Seventh AIAA CFD Drag Prediction Workshop

Edward N. Tinoco, Olaf P. Brodersen, Stefan Keye, Kelly R. Laflin, John C. Vassberg, Ben Rider, Richard A. Wahls, Joseph H. Morrison, Brent W. Pomeroy, David Hue, et al.

Summary Data from the Seventh AIAA CFD Drag Prediction Workshop

Edward N. Tinoco[1]
Retired, Kent, WA, 98031, USA

Olaf P. Brodersen[2] and Stefan Keye[3]
DLR Institute of Aerodynamics and Flow Technology, 38108 Braunschweig, Germany

Kelly R. Laflin[4]
Textron Aviation, Wichita, KS 67215, USA

John C. Vassberg[5],
JetZero, Huntington Beach, CA 92647, USA

Ben Rider[6]
The Boeing Company, Seattle, WA, 98124, USA

Richard A. Wahls[7]
NASA Headquarters, Washington, D.C. 20005, USA

Joseph H. Morrison[8], and Brent. W. Pomeroy[9]
NASA Langley Research Center, Hampton, VA 23681, USA

David Hue[10]
ONERA-The French Aerospace Lab, 92190 Meudon, France

and

Mitsuhiro Murayama[11]
Japan Aerospace Exploration Agency, Chofu, Tokyo 182-8522, Japan

Results from the Seventh AIAA CFD Drag Prediction Workshop – Expanding the Envelope – are presented. These cases focused on force/moment and pressure predictions for the NASA Common Research Model wing-body configuration. The Common Research Model geometry was deformed to the appropriate static aeroelastic twist and deflection at each specified angle-of-attack. The grid refinement study (Case 1) used a common set of overset, multiblock structured, and unstructured grids, as well as user created unstructured and structured based grids. Solutions were requested for the wing-body at a fixed Mach number and lift coefficient near buffet onset. The wing-body static aeroelastic/buffet study (Case 2)

[1] Boeing Technical Fellow (Retired), AIAA Associate Fellow
[2] Vice Director, DGLR Member
[3] Research Scientist
[4] Principal Engineer, AIAA Associate Fellow
[5] Chief Design Officer, Boeing Technical Fellow (Retired), AIAA Fellow, Chairman DPW
[6] Senior Engineer, AIAA Member
[7] Sustainable Flight National Partnership Mission Integration Manager - ARMD, AIAA Fellow.
[8] Chief Engineer for Modeling and Simulation, Research Directorate, AIAA Associate Fellow
[9] Configuration Aerodynamics Branch, AIAA Senior Member
[10] Research Engineer, Applied Aerodynamics Department.
[11] Senior Researcher, AIAA Senior Member

specified an angle-of-attack sweep at finely spaced intervals through the zone where wing shock-induced separation was expected to begin. Case 3 requested a Reynolds number/dynamic pressure sweep at a constant lift coefficient. The optional Case 4 requested grid adaption solutions of the wing-body at a specified flight condition. Optional Case 5 requested solutions beyond steady RANS. Optional Case 6 requested coupled aerostructural wing-body solutions. Results from this workshop highlight the progress made since the last workshop in 2016, and the continuing need for CFD improvement, particularly for conditions with significant flow separation, and close to buffet onset. These comparisons also suggest the need for improved experimental diagnostics to guide future CFD development.

I. Nomenclature

AMM-QCR	nonlinear two-equation k-ε turbulence model with Quadratic Constitutive Relation
AR	Wing Aspect Ratio
b	Wing Span
BL	Butt Line Coordinate (y)
C_D	Drag Coefficient (CD_TOT)
C_{DP}	Idealized Profile Drag = $C_D - C_L^2/\pi AR$
C_{Dpr}	Pressure Drag Coefficient (CD_PR)
C_{Dsf}	Skin-Friction Drag Coefficient (CD_SF)
C_L	Lift Coefficient (CL)
C_M	Pitching Moment Coefficient (CM, CM_TOT)
C_P	Pressure Coefficient (CP) = $(P-P_\infty)/q_\infty$
c_{ref}	Wing Reference Chord ~ MAC
C_f	Local Coefficient of Skin Friction
DES	Detached Eddy Simulation
EARSM	Explicit Algebraic Reynolds Stress turbulence model
FS	Fuselage Station Coordinate (x)
GRIDFAC	$N^{-2/3}$
HiQ	High dynamic pressure (Q)
LE	Wing Leading Edge
LoQ	Low dynamic pressure (Q)
MAC	Mean Aerodynamic Chord
N	Number of solution points (GRIDSIZE)
NoQ	No dynamic pressure (Q)
NTF	NASA National Transonic Facility (wind tunnel)
RANS	Reynolds-Averaged Navier-Stokes
RE	Chord Reynolds Number
RSM-ω	Reynolds-stress turbulence model with ω formulation
SA	Spalart-Allmaras turbulence model
SA-QCR	Spalart-Allmaras turbulence model with Quadratic Constitutive Relation
SSG/LLR	Speziale-Sarkar–Gatski/Launder–Reece–Rodi Reynolds-stress turbulence model
S_{ref}	Reference Area
SOB	Side-of-Body
TE	Wing Trailing Edge
TWT	NASA Ames Research Center Unitary Plan Wind Tunnel 11- by 11-Foot Transonic Wind Tunnel
URANS	Unsteady Reynolds-Averaged Navier-Stokes
WL	Water Line Coordinate (z)
w	Wing Section Bending Deflection
x/c	Wing Chord Fraction
y^+	Normalized Wall Distance
α	Angle-of-attack (ALPHA)
ε	Wing Section Twist Deflection
$\Lambda_{c/4}$	Quarter Chord Sweep
λ	Wing Taper Ratio
eta (n)	Fraction of Wing Semi-Span

II. Introduction

The AIAA CFD Drag Prediction Workshop (DPW) Series was initiated by a working group of members from the Applied Aerodynamics Technical Committee of the American Institute of Aeronautics and Astronautics. The primary goal of the workshop series is to assess the state-of-the-art of modern computational fluid dynamics methods using geometries and conditions relevant to commercial aircraft. From the onset, the DPW organizing committee has adhered to a primary set of guidelines and objectives for the DPW series:

- Assess state-of-the-art Computational Fluid Dynamics (CFD) methods as practical aerodynamic tools for the prediction of forces and moments on industry-relevant geometries, with a focus on absolute drag.
- Provide an impartial international forum for evaluating the effectiveness of CFD Reynolds Averaged Navier-Stokes solvers, as well as more advanced methods.
- Promote balanced participation across academia, government labs, and industry.
- Use common public-domain subject geometries, simple enough to permit high-fidelity computations but relevant for industry.
- Provide baseline grids to encourage participation and help reduce variability of CFD results.
- Openly discuss and identify areas needing additional research and development.
- Conduct rigorous statistical analyses of CFD results to establish confidence levels in predictions.
- Schedule open-forum sessions to further engage interaction among all interested parties.
- Maintain a public-domain accessible database of geometries, grids, and results.
- Document workshop findings; disseminate this information through publications and presentations.

Six previous workshops have been held prior to the present study, all held in conjunction with the AIAA Applied Aerodynamics Conference for that year.

Year	Location	Configuration	Case Descriptions
2001	Anaheim, CA	DLR-F4 Wing-Body	Single Point Drag Prediction Drag Polar Drag Rise Curves at Constant C_L*
2003	Orlando, FL	DLR-F6 Wing-Body Wing-Body-Nacelle	Single Point Grid Convergence Study Drag Polar Boundary Layer Trip Study* Drag Rise Curves at Constant C_L*
2006	San Francisco, CA	DLR-F6 Wing-Body with and without FX2B fairing; W1/W2 Wing Alone	Single Point Grid Convergence Study Drag Polar Grid Convergence Study Drag Polar
2009	San Antonio, TX	NASA Common Research Model Wing-Body and Wing-Body-Tail	Grid Convergence Study Downwash Study Mach Sweep Study* Reynolds Number Study*
2012	New Orleans, LA	NASA Common Research Model Wing-Body 2-D Flat Plate* 2-D Bump-in-channel* 2-D NACA 0012 Airfoil*	Grid Convergence Study Alpha Sweep Buffet Study Turbulence Model Verification*
2016	Washington DC	NASA Common Research Model Wing-Body and Wing-Body-Nacelle-Pylon 2-D NACA 0012 Airfoil	Grid Convergence Study Nacelle-Pylon Drag Increment Study Alpha Sweep Buffet Study Solution Adaption Grid Study* Coupled Aero-Structural Analysis Study* Turbulence Model Verification

*Optional Cases

While there have been some variations, the workshops have typically used subjects based on commercial transport wing-body configurations - a consensus of the organizing committee based on a reasonable compromise between simplicity and industry relevance. With very few exceptions the participants submit results generated with Reynolds Averaged Navier-Stokes (RANS) codes, although the organizing committee does not restrict the methodology.

The first Drag Prediction Workshop [1] used the DLR-F4 geometry for the above reasons and due to the availability of publicly released geometry and wind tunnel results [2]. The focus of the workshop was to compare absolute drag predictions, including the variation due to grid type and turbulence model type. The results were also compared directly to the available wind tunnel data. The workshop committee provided a standard set of Multiblock structured, overset, and unstructured grids for the DLR-F4 geometry to encourage participation in the workshop and reduce variability in the CFD results. However, participants were also encouraged to construct their own grids using their best practices so that learned knowledge concerning grid generation and drag prediction might be shared among workshop attendees. The test cases were chosen to reflect the interests of industry and included a fixed-C_L single point solution, drag polar, and constant-C_L drag rise data sets. To help encourage wide participation, a formal paper documenting results was not required at the workshop. Eighteen participants submitted results, using 14 different CFD codes; many submitted multiple sets of data exercising different options in their codes, e.g., turbulence models and/or different grids. A summary of these results was documented by the DPW-I organizing committee[3]. Because of strong participation, DPW-I successfully amassed a CFD data set suitable for statistical analysis [4]. However, the results of that analysis were rather disappointing, showing a 270-drag-count (a drag count = 0.0001 C_D) spread in the fixed-C_L data, with a 100:1 confidence interval of more than ±50 drag counts.

Despite the somewhat disappointing results, the consensus of the participants and organizers was that DPW-I was a definitive success. First and foremost, it was initiated as a "grass roots" effort by CFD developers, researchers, and practitioners to focus on a common problem of interest to the aerospace industry. There was open and honest exchange of common practices and issues that identified areas for further research and scrutiny. The workshop framework was tested successfully on high fidelity 3D RANS methods using a common geometry, grids, and test cases. Finally, it reminded the CFD community that CFD is not a fully mature discipline.

The interest generated from the workshop was continued and resulted in several individual efforts documenting results more formally [5-8], presented at a special session of the 2002 AIAA Aerospace Sciences Meeting and Exhibit in Reno, NV. The interest generated by DPW-I naturally led to the planning and organization of the 2nd AIAA Drag Prediction Workshop, DPW-II. The DPW-II organizing committee, recognizing the success of DPW-I, maintained the format and objectives for DPW-II.

The second workshop [9] used the DLR-F6 as the subject geometry in both wing-body (WB, like DLR-F4) and wing-body-nacelle-pylon (WBNP) form. The DPW-II organizing committee worked with DLR and ONERA to make pertinent experimental data available to the public domain. One specific objective of DPW-II was the prediction of the incremental drag associated with nacelle/pylon installation. The F6 geometry contained known pockets of flow separation more severe than the F4, occurring predominantly at the wing/body and wing/pylon juncture regions. The results from the workshop were documented with a summary paper [10], a statistical analysis [11], an invited reflections paper [12] on the workshop series, and numerous participant papers [13-21] in two special sessions of the 2004 AIAA Aerospace Sciences Meeting in Reno, NV. A conclusion of DPW-II was that the separated flow regions made it difficult to draw meaningful conclusions with respect to grid convergence and drag prediction. During the follow-up open-forum discussions, the CFD community voiced the desire for the organizing committee to include in the third workshop: a) Blind Test Cases, and b) Simpler Geometries. The request for blind test cases is motivated by an earnest attempt to better establish a measure of the CFD community's capability to predict absolute drag, rather than match it after-the-fact. The request for simpler geometries allows more extensive research in studies of asymptotic grid convergence.

The third workshop [22] retained the DLR-F6 WB from DPW-II as a baseline configuration to provide a bridge to the previous workshop. However, to test the hypothesis that the grid-convergence issues of DPW-II were the direct result of the large pockets of flow separation, a new wing-body fairing was designed to eliminate the side-of-body separation. Details of the FX2B fairing design are documented by Vassberg [23]. In addition, to help reduce the wing upper-surface trailing-edge flow separation, a higher Reynolds number was introduced for the WB test cases. These changes in both geometry and flow condition also provided the

DPW-III participants a blind test since no test data would be available prior to the workshop. Furthermore, two wing-alone geometries were created to provide workshop participants with simpler configurations on which more extensive grid-convergence studies could be conducted; these wings were designed to exhibit no appreciable separation at their design conditions. The DPW-III was heavily documented with summary papers [24,25], a statistical analysis paper [26] participant papers [27-30], and a special section of the AIAA *Journal of Aircraft*, edited by Vassberg [31-36]. After three workshops, the organizing committee recognized that a recurring theme of the workshop series was related to grid quality and resolution – see Mavriplis et al. [37]

For the fourth workshop [38] a completely new geometry was developed, called the Common Research Model (CRM). The NASA Subsonic Fixed Wing (SFW) Aerodynamics Technical Working Group (TWG), in collaboration with the DPW Organizing Committee, developed the CRM. This wing-body (with and without nacelle-pylons and horizontal tail) configuration is representative of a contemporary high-performance transonic long-range transport. A detailed description of its development is given by Vassberg et al. [39]

One aspect of DPW-IV different from the other workshops was in the timing of the availability of wind-tunnel test data on the subject geometries. In DPW-IV, the workshop was held before any experimental data were collected and is a set of blind tests. Due to past observations of grid dependence on the solutions, a greater emphasis was placed on establishing a comprehensive set of meshing guidelines for the generation of baseline grid families. With these guidelines in place, grids were requested from several organizations for structured multiblock, overset, and unstructured types. Each grid family was required to include a Coarse (C), Medium (M), and Fine (F) grid; adding an optional Extra-Fine (X) grid was also encouraged. Target sizes for these grids were 3.5, 10, 35, and 100 million solution points, respectively. The Medium mesh was intended to be representative of current engineering applications of CFD being used to estimate absolute drag levels on similar configurations. A total of 74 meshes of 18 families were provided and made available to participants for use.

The fourth workshop requested grid convergence and Mach sweep computations as in the previous workshops, plus downwash and Reynolds Number studies. Data were submitted from 19 organizations totaling 29 individual datasets. For the grid refinement study, a Richardson Extrapolation methodology [40] was employed to estimate a continuum value for the total drag coefficient. Excluding a single outlier, the scatter band for DPW-IV reduces dramatically to 41 counts, which is a definite improvement over DPW-I (with one outlier, the range for the total drag coefficient spanned 152 counts). While this improvement is quite significant, the confidence level is not down to a low enough level to compete with experimental methods. Documentation for these results can be found in summary papers [40-41] and in individual contributing papers [42-56] from two special sessions held at the 28th Applied Aerodynamics Conference in June 2010.

Despite the emphasis placed on grid generation with the intent of reducing the associated errors, the variation in the DPW-IV results was still disappointing. For the fifth workshop [57], which was held in conjunction with the 30th AIAA Applied Aerodynamics conference in June 2012, a new approach was taken with the goal of reducing grid-related errors even further. As with the fourth workshop, the NASA Common Research Model wing body configuration was used for the geometry (without tail). For the grids, a unified baseline [58] family of Multiblock structured meshes was developed with six different levels ranging in size from 0.64×10^6 (Tiny) to 136×10^6 (Superfine) mesh points. Each successive coarse level was derived directly from the finest mesh. Only five blocks were used. Once the cloud of points was defined for this series of grids, then Overset and Unstructured grids were derived. The unstructured grids were defined in Hexahedral, and Prismatic elements, plus a hybrid grid with Prismatic boundary layer and Tetrahedral field elements was defined.

The test cases included a grid refinement study using the common grids or user-supplied custom grids if desired. The second case focused on buffet prediction, with a finely spaced alpha sweep spanning the range where flow separation on the wing was observed in the wind tunnel data and the results in DPW-IV. This was a change from previous workshops, where angle-of-attack sweeps from 0° to 4° were calculated for the purpose of determining trimmed drag polars. For a commercial transport like the CRM, high-speed lines development is undoubtedly very important, as it would contribute to whether speed and range goals are met. However, it usually comprises less than 25% of the total aerodynamics-related airplane development effort. Significant effort must also be paid to loads, handling qualities, and other constraints that are required to meet structural and certification requirements. Many of these high-speed flight concerns occur at the edges of the

flight envelope, which are characterized by large regions of separated flows, including shock-induced separation on the wing. For the Fifth Drag Prediction Workshop, the buffet study was included to assess CFD prediction in this regime. The optional third test case used geometries, grids, and conditions from the Turbulence Model Resource website [59] prepared by the Turbulence Model Benchmarking Working Group. Three verification [96] cases were selected: 1) 2D Zero Pressure Gradient Flat Plate, 2) 2D Bump-in-channel, and 3) 2D NACA 0012 Airfoil. These test cases were designed to discriminate between turbulence model implementations through rigorous grid convergence studies. Documentation for these results can be found in summary papers [60-61] and in individual contributing papers [62-70] from two special sessions held at the 51st Aerospace Sciences Meeting, January 2013, the 52nd Aerospace Sciences Meeting, January 2014, and a special collection in the AIAA *Journal of Aircraft* [71].

The Sixth Drag Prediction Workshop [72] was held in conjunction with AIAA Aviation 2016 and included 25 participant teams from 4 continents representing government, industry, academic, and commercial CFD organizations. The workshop again focused on the CRM model and the NACA 0012 airfoil. Five cases were specified. Case 1 featured detailed grid convergence studies for drag and skin friction coefficient for the Turbulence Modeling results based on the NACA 0012 airfoil [73]. Cases 2-5 involved the CRM model. An overview of the computational results, geometry, and grid definitions used for the CRM cases are presented in Ref. 74. For the CRM, four case studies were specified, two of which were optional. The required cases included a grid refinement study using the common grids or user-supplied custom grids for both the Wing-Body (WB) and Wing-Body-Nacelle-Pylon (WBNP) configurations (Case 2), and a WB angle-of-attack sweep with a finely spaced alpha sweep spanning the range where flow separation on the wing was observed in the wind tunnel data similar to that in DPW-V (Case 3). New for DPW-VI was the inclusion of the static aeroelastic deformation in the definition of the CRM models for each angle-of-attack/C_L condition specified in the test cases. This makes comparisons to force, moment, and pressure data from the related wind tunnel tests more meaningful in that the geometry of the computational model better represents that of the wind tunnel model at the specified flow condition. The Case 2 grid refinement study consisted of up to 7 levels of grid sizes ranging from 7.4 to 225 million control volumes. Richardson extrapolation was used to estimate the continuum force levels and the drag increment between the two configurations. This showed that the scatter band of results in the continuum to be further reduced from that seen in previous workshops. Results of a statistical analysis of Case 2 are presented in Ref. 75. Analysis of the Case 3 static aeroelastic/buffet study including force/moment and pressure predictions with comparisons to wind tunnel test data was like that seen in DPW-V, but with fewer outliers. Few participants submitted results for the two optional cases: Case 4 grid adaptation, and Case 5 coupled aerostructural simulation. A detailed description of Case 5 results can be found in Ref. 76. Additional documentation for these results can be found in individual contributing papers in a special collection in the AIAA *Journal of Aircraft* [77-85].

This paper presents an overview of the computational results, geometry, and grid definitions used in the Seventh Drag Prediction Workshop–Expanding the Envelope (DPW-VII) [86]. The workshop was held in conjunction with AIAA Aviation 2022 Conference held in Chicago, Il. and included 18 participant teams from 3 continents representing government, industry, academic, and commercial CFD organizations. The workshop again featured the NASA High Speed CRM model. A primary focus of this workshop was on predicting the effect of shock-induced separation on the variation of lift and pitching moment with increasing angle-of-attack at transonic conditions. In DPW-VI only 5 out of 41 solutions submitted adequately predicted this variation [87]. Flow conditions dominated by shock-induced separation represent a significant portion of the flight regime critical to safety and government certification regulations. All too often, anomalies in this flight regime are not discovered until flight test resulting in expensive and time-consuming campaigns to "fix" the issue. Wind tunnels typically cannot simulate the flight Reynolds number and the various aircraft aeroelastic deformations over the range of interest. CFD can contribute if it can be shown to adequately model the development and progression of shock-induced separation with increasing angle-of-attack. The variation of pitching moment with angle-of-attack is a most sensitive indicator in that not only must the lift be adequately predicted but also its distribution with increasing flow separation. This is a sensitive demonstration of CFD accuracy in predicting this critical behavior. As was done in DPW-VI is the inclusion of the static aeroelastic deformation in the definition of the CRM models for each angle-of-attack/C_L condition specified in the test cases.

Key objectives of DPW-VII included:

1) Assessment of grid convergence characteristics a higher lift coefficient close to the pitching moment break.
2) Focus on characteristics at Re=20M in addition to Re=5M of previous workshops
3) Assessment of characteristics beyond the pitching moment break that are subject to strong shock-induced separation.
4) Assessment of Grid Adaptive Technology
5) Assessment of higher order CFD methods
6) Assessment of Coupled Aerostructural Simulation

Six case studies were specified, three of which were optional. The six test cases are described in more detail in Section IV of this paper. Briefly, Case 1 focused on a grid convergence study at a higher lift coefficient than specified for previous workshops featuring the CRM. Cases 2, 4, 5, and 6 addressed characteristics over a range of angles-of-attack which included predicting the effect of shock-induced separation on the variation of lift and pitching moment with increasing angle-of-attack. Case 3 featured a Reynolds number/dynamic pressure sweep. Of the optional cases: Case 4 focused on grid adaptation; Case 5 called for solutions based on solvers beyond steady RANS, unfortunately insufficient results were submitted to draw any firm conclusions; Case 6 featured coupled aerostructural simulation. Results from these cases are described in Section V of this paper.

III. Geometry and Experimental Data Description

The subject geometry for DPW-VII is the Common Research Model [39] (CRM) developed jointly by the NASA Subsonic Fixed Wing (SFW) Aerodynamics Technical Working Group (TWG) and the DPW Organizing Committee. The CRM was designed as a full configuration with a low wing, body, horizontal tail, and engine nacelles mounted below the wing. For this workshop, only the wing-body configuration was used because the focus was on the wing aerodynamic characteristics. A rendering of the wing-body configuration geometry is shown in Fig. 1, along with a photo of the 0.027 scale wing-body wind tunnel model in the NASA NTF. The CRM was also the subject geometry for DPW-IV through DPW-VI.

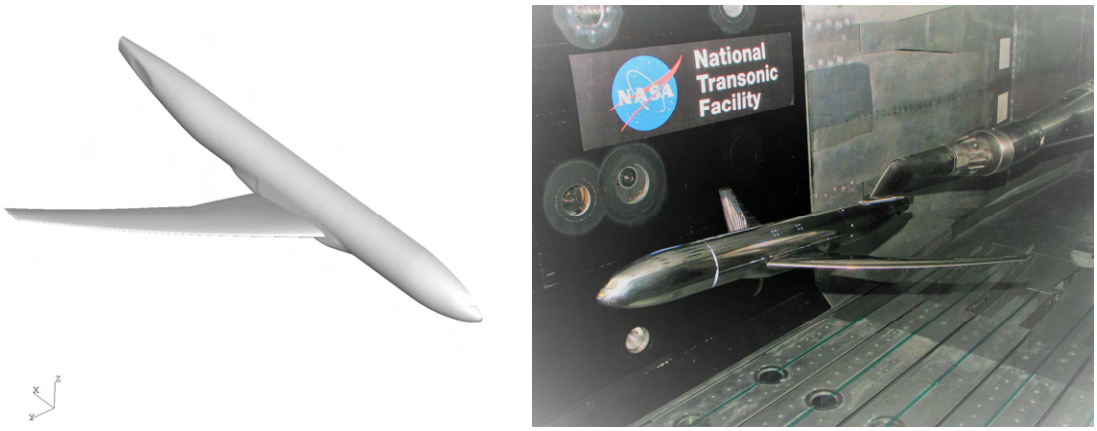

Fig. 1 NASA Common Research Model (CRM) geometry for DPW-VII

The wing is designed for a nominal condition of Mach=0.85, C_L=0.50, and Reynolds Number 40×10^6 based on c_{ref}, which is typical for a full-size commercial transport. Pertinent geometric parameters are listed in Table 1. The wing is a supercritical design, and the Boeing Company took the lead on the aerodynamic design [39]. Certain features are designed into the wing profile for the purposes of research and development. For example, the upper-surface pressure recovery over the outboard wing is intentionally made aggressively adverse over the last 10-15% local chord. This promotes separation of the upper-surface boundary layer in close proximity to the wing trailing edge (TE) at lift conditions slightly above the design point. The strong adverse pressure gradient will likely amplify the differences in various turbulence models that may be

employed by DPW participants. Another feature is that the span loading is designed to be very nearly elliptical as compared to a more practical design that would use a compromise distribution (more triangular) to reduce structural loads and decrease airframe weight. This feature is included to provide a challenge for possible future workshops on aerodynamic shape optimization that might explore structure and fuel weight trade-offs.

Table 1. Reference quantities for the CRM (Full Scale).

S_{ref}	594,720.0 in^2	= 4,130 ft^2 [458.89 m^2]	x_{ref}	1,325.9 in	[33.68 m]
S_{trap}	576,000.0 in^2	= 4,000 ft^2 [444.44 m^2]	y_{ref}	468.75 in	[11.91 m]
b	2,313.5 in	= 192.8 ft [58.765 m]	z_{ref}	177.95 in	[4.520 m]
c_{ref}	275.800 in	= 16.07 ft [4.8978 m]	$\Lambda_{c/4}$	35.0°	
AR	9.0		λ	0.275	

In assessing the accuracy of CFD, wind tunnel results are frequently used as the "gold standard." However, even if we had the perfect representation of flow physics in a CFD code, we would not, nor should we get perfect agreement with wind tunnel results, because the wind tunnel is also imperfect. Each wind tunnel experiment has its own imperfections, which must be understood or at least recognized in order to assess or validate the CFD. Generic differences in the "test" setup between Wind Tunnel and CFD are well known, and a few are listed below:

Wind Tunnel	**CFD**
Walls	Free Air
Support System (Sting)	Free Air
Laminar/Turbulent (Tripped @ 10% chord)	"Fully" Turbulent Specified (usually)
Aeroelastic Deformation	Specified Shape (except Case 6)
Measurement Uncertainty	Numerical Uncertainty and Error
Corrections for known effects	No Corrections

With this approach, physical experiments are adjusted/corrected to approximate free air conditions while the CFD also simulates free-air conditions. Free-air conditions are conducive to the numerical assessments of DPW. For comparisons with experiment, it is becoming a common practice to simulate more of the test environment with CFD (e.g., support system, static aeroelastics) and incorporate correspondingly less corrections in the data. Support system simulations [88] and static aeroelastic deformation effects are two examples of this trend.

Clearly there are potentially significant differences between what Wind Tunnel and CFD are measuring/computing. Effective CFD assessment requires intimate knowledge of both the CFD, and the experimental data being compared. CFD assessment cannot consist of the comparison of the results of one code to those of one experiment. Rather, it is the agglomeration of comparisons at multiple conditions, code-to-code comparisons, an understanding of the wind tunnel corrections, etc., that leads to the understanding of the CFD for use as an engineering tool.

An advantageous outcome of the collaborative endeavor sponsored by the NASA Aerodynamics Technical Working Group (TWG) has been that the CRM has now been tested in several facilities thus far, and the data from several of these tests are now publicly available. The National Transonic Facility (NTF) at NASA Langley tested the CRM during January - February 2010, followed by a test at the NASA Ames 11-Foot TWT (Unitary Plan Wind Tunnel 11- by 11-Foot Transonic Wind Tunnel) during March - April 2010. Data from the Langley and Ames tests have been released to the public domain by Rivers and Dittberner [88-90]. The CRM Wing-Body configuration was tested at the European Transonic Wind Tunnel (ETW) facility in February 2014 [91]. These data have also been released to the public domain [92]. These three tests all used the same physical wind tunnel model. A slightly larger version of the CRM Wing-Body-Tail was built by ONERA and tested in the ONERA S1MA wind tunnel [83]. In 2012, an 80% scale model of the NASA CRM built by JAXA was tested in the JAXA 2m x 2m Transonic Wind Tunnel [92].

A comparison of data from the various wind tunnels shows that the wing pressure distributions are virtually indistinguishable at the conditions specified for DPW-VII. Whether this is true for other conditions has not been checked in detail. Force and pitching moment data from the different wind tunnels do differ. It

is believed that these differences are mainly due to the corrections applied to the "raw" measured data to account for wind tunnel walls, mounting system, non-uniform flow (buoyancy, upflow, etc.), Mach blockage, lift interference, etc. Each wind tunnel facility tries very hard to determine the "best" set of corrections to its data to simulate "free air". The CRM test data do not include mounting system corrections. Mounting system effects, which require a special set of "tare and interference" tests to determine, are usually not included in the standard set of corrections applied to the wind tunnel data. Computational studies by Rivers, Hunter, and Campbell [94-95] and discussion by Pfeiffer [12] illustrated the magnitude of the mounting system influence on the CRM Wing-Body-Tail configuration. Because of the flow anomalies present in every wind tunnel and the approximate nature of the corrections applied to account for these irregularities, the absolute measurement of forces and moments corresponding to "free air" is impractical if not impossible. It is therefore not unusual that the drag levels will differ between wind tunnels.

Today's CFD allows modeling of turbulence and transition with different level of fidelity. Running CFD fully turbulent (as was mostly done in DPW series) means that at low Reynolds number (Re=5M) neither the benefit of the laminar run prior to the trip, nor the added drag and increased boundary layer thickness due to the trip will be accounted for. This may be less of an issue at higher Reynolds number with smaller laminar runs and no trip on the wind tunnel model. Perhaps when direct numerical simulation of the Navier-Stokes equations is possible for complex configurations at high Reynolds number an improved calculation of absolute forces and moments will be possible. However, the calculation or measurement of increments between two similar configurations should certainly be feasible with carefully executed wind tunnel test programs and CFD. For comparison purposes, test data from the NASA 11-Foot TWT and NTF tests will be used. The same physical model of the Wing-Body configuration of the was tested in these two tunnel facilities.

The inclusion of the static aeroelastic deformation in the definition of the CRM models for each angle-of-attack/C_L condition specified in the test cases. The wing static aeroelastic bending and twist deflection were derived using a videogrammetry technique in which the position of markers on the wing was measured during the test. The bending and twist deflection used to define the geometries for DPW-VI were based on data measured in the ETW test in 2014. While the test results from the ETW test and those from the NASA NTF and 11-Foot TWT tests were quite similar, it was decided to use the ETW results. These data were interpolated to the angles-of-attack required in test cases 1 to 6 to define the various geometries [96]. Static aeroelastic wing twist for various angles-of-attack is shown in Fig. 2. Note that the resulting aeroelastic twist is small, amounting to only a little over one degree near the wing tip. However, at transonic flow conditions, this small amount of aeroelastic wing twist has a significant effect on the resulting pressure distributions as shown in Fig. 3 for two spanwise locations. Computed lift, drag, and pitching moment are also affected. Inclusion of the aeroelastic deformation makes comparisons to force, moment, and pressure data from the related wind tunnel tests more realistic in that the geometry of the computational model better represents that of the wind tunnel model at the specified flow condition.

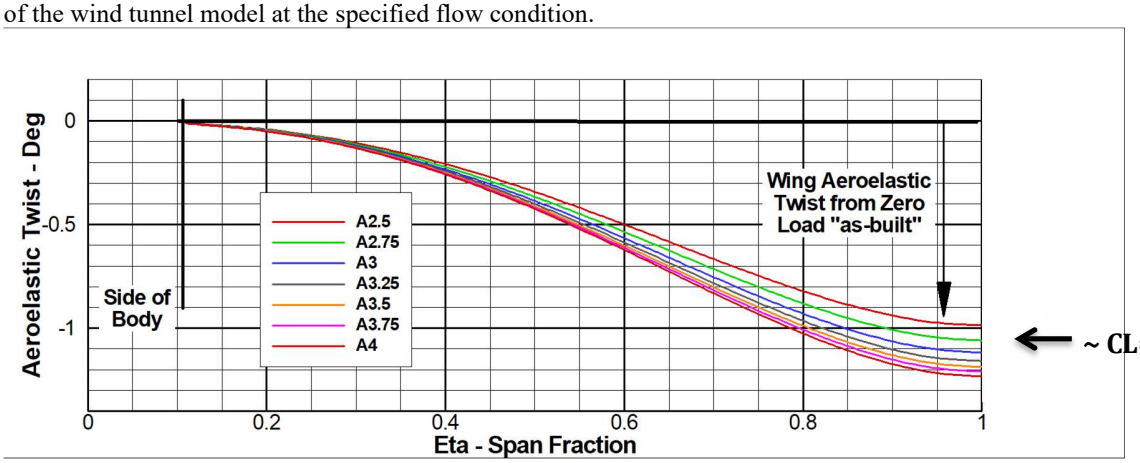

Fig. 2 Static Aeroelastic Twist Distributions Derived from Wing Tunnel Measurements.

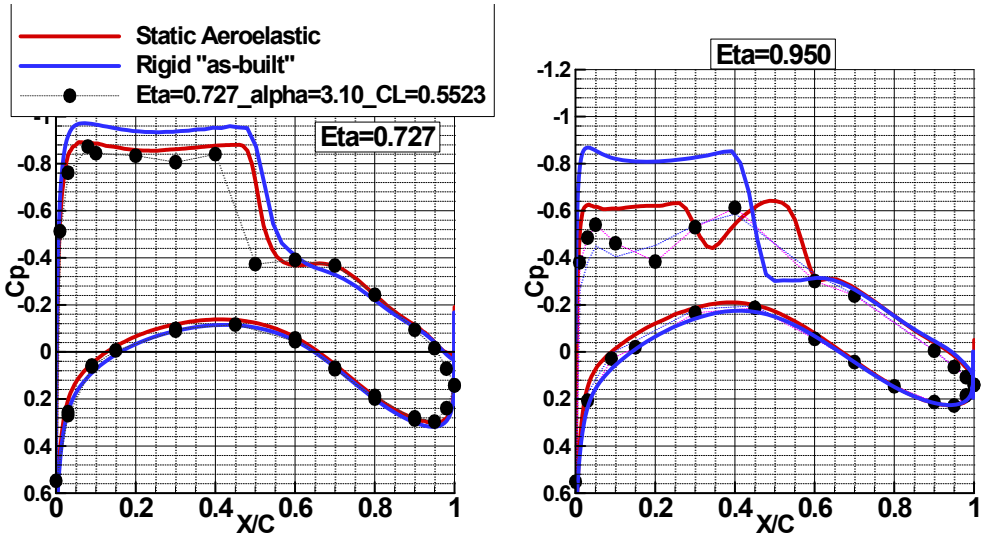

Fig. 3 Impact of Static Aeroelastic Deformation on Wing Pressure Distributions – 3° Angle-of-Attack – Lines: CFD and Symbols: Experiment.

Limitations in the total number of pressure taps that can be built into the wind tunnel model and subsequent plugged and/or "slow" taps may result in inadequate definition of the experimental pressure distributions at the various span stations. This is particularly the case in defining the wing shock location in transonic flow and adequately defining the aft loading near the wing trailing edge. For attached flow conditions, there is very little change in the pressures with angle-of-attack near the wing trailing edge as long as the flow remains attached. In order to calculate section lift and moment characteristics, it was necessary to "enhance" the experimental pressure distributions. The "enhancement" to the pressures near the wing trailing edge was based on a combination of interpolation/extrapolation guided by experience with test data and CFD. At three midspan stations, missing or very "slow" taps required a further "enhancement." These "enhanced pressures" were based on pressure measurements from the JAXA 80% CRM model, which did not suffer these particular pressure tap manufacturing deficiencies. An example of these enhancements is shown in Fig. 4 for two spanwise stations. The original pressure data are shown by the open symbols, the enhanced distributions, which include the original data points, are shown by the solid symbols.

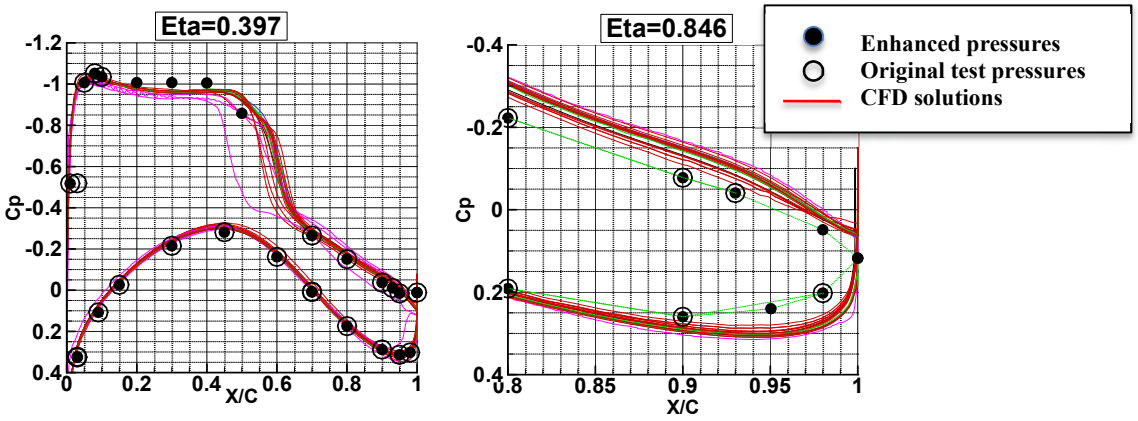

Fig. 4 Enhancement of Wing Tunnel Pressure Measurements.

III. Gridding Guidelines and Description of Common Grids

Since the establishment of the Drag Prediction Workshop Organizing Committee in 2000, the DPW-OC has deemed it essential to provide a set of baseline grids on which DPW Participants are to conduct their CFD analyses on workshop test cases. While custom grids are also encouraged, the baseline grids are intended to provide high-quality meshes with a measure of consistency across grid types and family members. In this context, grid types include multiblock, overset, unstructured and hybrid meshes, while a grid family consists of parametrically-consistent meshes of varying grid resolution to be used for grid-convergence studies. Custom grids are encouraged to help bring additional best practices into the public domain to advance the state-of-the-practice in grid generation for RANS simulations. Consistency across baseline meshes is established by use of a set of gridding guidelines.

A. Gridding Guidelines

The gridding guidelines established for the CRM wing-body configuration of DPW-VII are listed in Table 2 below. The guideline list anchors characteristics for the smallest grid member of the grid-convergence family, referred to as the *Tiny Grid* or *L1 Mesh* or simply *L1.T*. Note that we set the viscous-wall spacing to be approximately $Y^+ \sim 1$, and we request that at least the first two cells are constantly spaced with $\Delta y_1 = \Delta y_2 = 0.0002332$ inches for the full-scale CRM geometry. Also on the *Tiny Grid*, we request that the growth rates in the viscous-wall-normal direction not exceed a stretching ratio of 1.20; as this mesh gets refined from *L1*-to-*L6*, the growth rates naturally reduce and approach unity. The farfield boundary should be at least 100 characteristic lengths away from the geometry. Grid size ratios between family members are also given to help manage the magnitude of the largest mesh.

Table 2. List of Gridding Guidelines

- **Tiny Grid (L1.T)**
  - Viscous Wall Spacing: $Y^+ \sim 1.0 \rightarrow \Delta y_1 = 0.0002332$”
    - Based on local C_f @ 10% Cref for $Re_c = 30$ million
    - $C_f \sim 0.455 / \ln^2(0.06*Re_x) = 0.003107$, where $Re_x = 0.1*Re_c = 3$ million
    - $\Delta y_1 =$ Cref / $[Re_c*\text{sqrt}(C_f/2)] = 0.0002332$”
  - At Least 2 Constantly-Spaced Cells at Viscous Walls, $\Delta y_2 = \Delta y_1$
  - Growth Rates < 1.2X Normal to Viscous Walls
  - Wing Spanwise Spacing < 0.1%*Semispan at Root & Tip
  - Wing Chordwise Spacing < 0.1%*C (Local Chord) at LE & TE
  - Wing TE Base >> 8 Cells
  - Spacing Near Fuselage Nose & End-of-Body < 1%*Cref
- **Grow Next-Finer Grid in Family by ~ $[(L+2)/(L+1)]^3$ in Size**
  - Scale Dimensions in All Three Directions by ~ [(L+2)/(L+1)]
  - Grid Spacings Should Reduce as follows, (0.1% in Tiny Grid)
    - [T,C,M,F,X,U] = [0.100, 0.067, 0.050, 0.040, 0.033, 0.029]%
- **Farfield Boundary > 100*Semispans**
- **Miscellaneous Notes:**
  - Try to be Multigrid Friendly on Structured Meshes
  - Store Grid Coordinates in 64-bit Precision
  - If Storing Grids in Plot3D Format, Keep Zones < 38M Nodes
  - Itemize Surface Elements by Components [W, B, Sym, Far]
  - Itemize Element Count for Unstructured Meshes
    - Volume: Tetrahedra, Prisms, Pyramids, Hexahedra
    - Surface: Triangles, Quads
  - Total of 15 Grids Needed per Grid Type
    - Subtotal of 8 AE Medium Grids @ Low-Q for Alpha Sweep
    - Subtotal of 1 AE Medium Grid @ High-Q for Q Effect
    - Subtotal of 1 Medium Grid on Undeflected Geometry for Case 6
    - Subtotal of 6 Grids in Grid Family for Grid Convergence
      - AE3.00degLoQ Geometry, CL = 0.58, Re = 20M, (Re = 5M Optional)

In order to satisfy the requirements of all DPW-VII Test Cases, a total of 15 grids per grid type is requested. This minimal set include 8 medium *L3.M* grids for the aero-elastic (AE) deformations of an Alpha sweep at a low dynamic pressure (LoQ), 1 AE *L3.M* grid at a high dynamic pressure (HiQ), 1 undeflected (NoQ) *L3.M* grid, and the 6 members of the grid family (*L1-L6*).

Table 3 provides key metrics for the DPW-VII Baseline Grid Families and how they should vary with grid refinement to yield a parametrically-consistent family. Six members of this family are requested. The requested family should span grid sizes from 5 million cells to 215 million elements. This constitutes a growth of ~40X from smallest-to-largest grid with 6 meshes, which is a manageable range, yet will provide rich content for grid-convergence studies. Note how Δy_1 and Y^+ vary with grid refinement.

Table 3. Guidelines for Baseline RANS Grid Family Plan

Name	L	WB	Δy_1	Y^+	$^{\#}\Delta y_1 s$
Tiny (T)	1	~5	0.0002332”	~1.00	2
Coarse (C)	2	~17	0.0001555”	~0.67	3
Medium (M)	3	~40	0.0001166”	~0.50	4
Fine (F)	4	~78	0.0000933”	~0.40	5
Extra Fine (X)	5	~135	0.0000777”	~0.33	6
Ultra Fine (U)	6	~215	0.0000666”	~0.29	7

Rough Nominal Size of Grid System in M-DOF

At Least 4 Sequential Mesh Levels & Bias Towards Finest

B. Vassberg Grids

A most comprehensive and versatile baseline grid family was provided by Vassberg. (Further, it provides a direct tie to the unified grids from DPW-V of 2012; the *L3.M* mesh here is almost identical to the *L5.X* from DPW-V, only the viscous-wall spacings differ.) As provided, these grids are directly applicable for both multiblock (MB) and overset (OS) RANS flow solvers. In addition, they can be easily converted to fully unstructured hexagons, prisms, or tetrahedra meshes.

Vassberg provided a set of 102 grids (matrix of 8 AE deflections, by 6 family members, by 2 dynamic pressures, plus 6 undeflected family members). Each grid consists of 5 multiblock zones and 4 overset bridging grids. All interfaces are point-matched across internal boundaries.

Table 4. summarizes the grid sizes and viscous-wall metrics of the Vassberg grid family. Note that these metrics closely match those set forth by the gridding guidelines described in the previous subsection. Here, the *Tiny Grid (L1.T)* has 5,286,597 grid points, while the largest *Ultra-Fine (L6.U)* grid is comprised of 221,294,757 vertices.

Table 4. Vassberg Grid Family Data

Name	L	WB	Δy_1	Y^+	$^{\#}\Delta y_1 s$
Tiny (T)	1	5,286,597	0.0002332”	~1.00	2
Coarse (C)	2	17,644,325	0.0001555”	~0.67	3
Medium (M)	3	41,590,149	0.0001166”	~0.50	4
Fine (F)	4	80,957,925	0.0000933”	~0.40	5
Extra Fine (X)	5	139,581,509	0.0000777”	~0.33	6
Ultra Fine (U)	6	221,294,757	0.0000666”	~0.29	7

Figure 5 provides a standardized quad-plot of grid images to help convey the grid topology of the Vassberg grid system. There are 5 basic multiblock zones – fuselage forebody, mid-section & afterbody, plus inboard & outboard wing blocks. The grid about wing airfoil sections are O-meshes. The symmetry plane is an O-mesh about the fuselage crown/keel perimeter. The surface mesh is extruded outward to a hemispherical farfield boundary. Grids are stored in a 64-bit plot3d grid format with a naming convention as follows. Grid levels include: *L1.T, L2.C, L3.M, L4.F, L5.X* and *L6.U*. AE deflections include: *HiQ, LoQ* and *NoQ*. Alpha conditions include: *A250, A275, A300, A325, A350, A375, A400,* and *A425*. For example, *L1.T.HiQ.A325.MB5.p3d* contains the *L1 Tiny* multiblock grid for the AE-deflected geometry at the conditions of high dynamic pressure and 3.25° angle-of-attack. If an overset grid is desired, add the corresponding *L1.T.HiQ.A325.OS4.p3d* grid file to the setup. These grids are available for download at the DPW-VII website [86].

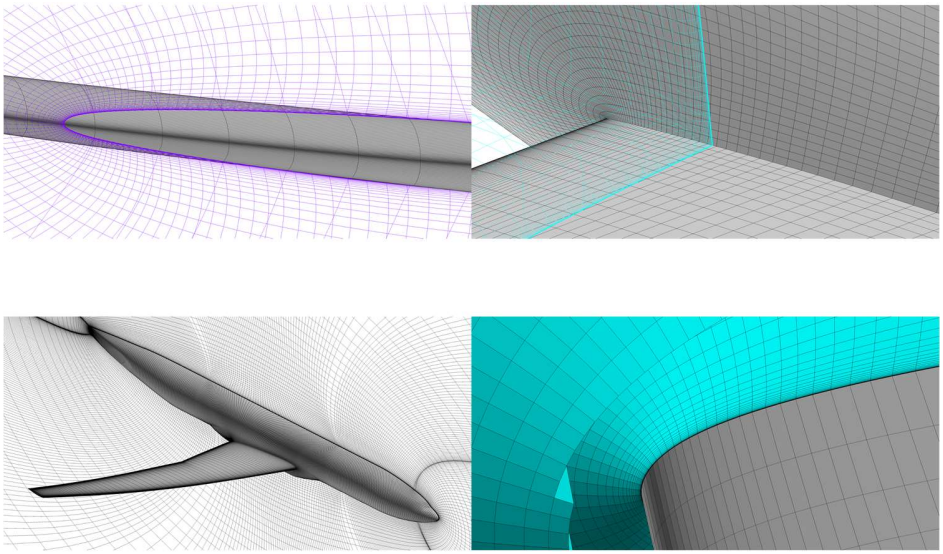

Fig. 5. Vassberg Grid Topology (Multi-Block & Overset)

C. NLR Grids

Another baseline grid is provided by the NLR. The grid topology of this multiblock structured mesh is more typical of most meshing software than that of Vassberg's grid system. Figure 6 provides the standardized quad-plot of grid images for comparison. Note that the symmetry plane on the NLR grid exhibits a "streamline" or H-mesh topology. The close-up view in the bottom-right quad illustrates that the wing is wrapped with a local body-conforming O-mesh, which is then surrounded by H-mesh topological blocks extending to the farfield boundaries. The top-right quad shows that the viscous sublayer at the wing-fuselage juncture is singularly clustered to manage grid count. The surface geometry, symmetry plane, and farfield boundaries are fully defined with quadrilateral elements.

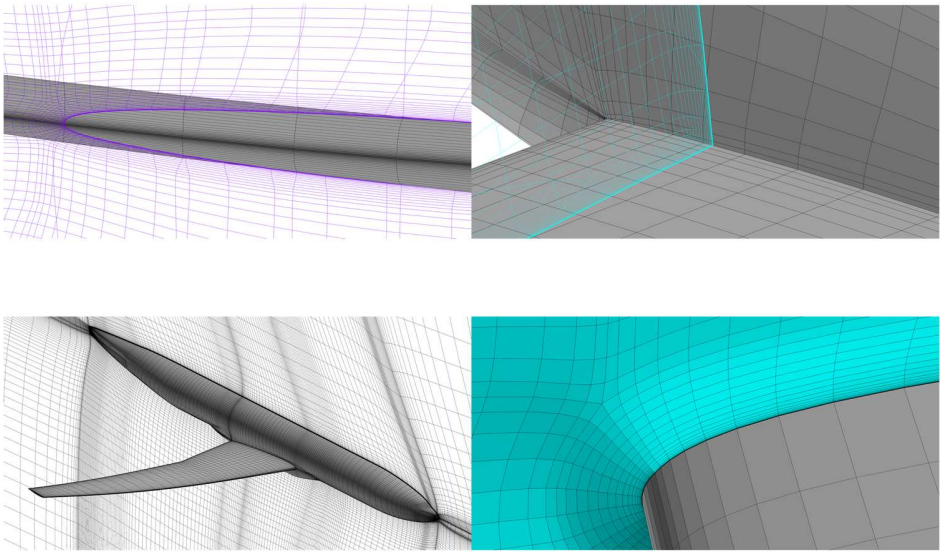

Fig. 6. NLR Grid Topology (Multi-Block).

D. JAXA Grids

Baseline hybrid unstructured meshes provided by JAXA were generated using the Mixed-Element Grid Generator in 3 Dimensions (MEGG3D) [97, 98]. Focus on the surface meshes of Fig. 7. Notice that the geometry is captured by a tessellation of predominantly triangles yet include quadrilaterals near the leading and trailing edge regions. These surface elements are extruded into the viscous sublayer to form mostly prisms and hexahedra. Beyond the sublayer the volume grid is comprised mainly of tetrahedra after the hexahedra are transitioned with a layer of pyramid elements. The crinkle surface (teal color) of the bottom-right quad image clearly illustrates this transition of hybrid elements from the viscous sublayer to the outer inviscid flowfield domain. Table 5 summarizes the grid sizes and viscous-wall metrics of the JAXA grid family. Note that these metrics closely match those set forth by the gridding guidelines and Vassberg Grids described in the previous subsections. Here, the *Tiny Grid (L1.T)* has 8,698,930 grid points, while the largest *Ultra-Fine (L6.U)* grid is comprised of 291,199,659 grid points.

Table 5. JAXA Grid Family Data

Name	L	No. Points	No. Elements	Δy_1	Y^+	Max. growth rate in boundary layer cells
Tiny (T)	1	8,698,930	25,294,690	0.0002332”	~ 1.00	1.323
Coarse (C)	2	26,891,512	76,058,884	0.0001555”	~ 0.67	1.205
Medium (M)	3	60,184,023	164,065,758	0.0001166”	~ 0.50	1.150
Fine (F)	4	111,843,367	295,240,476	0.0000933”	~ 0.40	1.118
Extra Fine (X)	5	184,127,176	476,358,610	0.0000777”	~ 0.33	1.098
Ultra Fine (U)	6	291,199,659	739,171,907	0.0000666”	~ 0.29	1.083

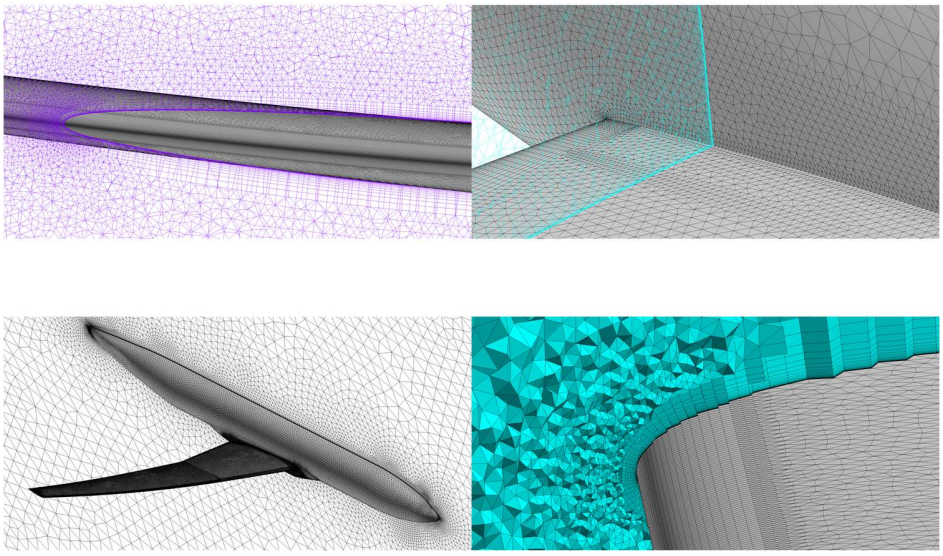

Fig. 7. JAXA Grid Topology (Mixed Unstructured Elements)

E. DLR Grids

DLR's custom-built CFD grids were generated using the commercial grid generation package SOLAR V15.3.8 [99] for building unstructured, hybrid meshes. In the boundary layer mesh predominantly hexahedra-type elements are used, while the farfield mesh is built from tetrahedral elements. Grids were generated for Test Cases 1a, 2a, and 6, and provided as common grids on the DPW-7 website [86] for free usage by workshop participants.

Test Cases for the workshop are described in Section IV. For Test Case 1a a baseline grid family consisting of six mesh levels L was required, with a size factor of $[(L+2)/(L+1)]^3$ in terms of total number of points between consecutive levels (Table 2). Specified values for Δy_1 lead to $y^+ \sim 1$ for the flow conditions defined for the Test Cases. Six grid levels with spatial resolutions ranging from Tiny (T) up to Ultra Fine (U) were generated on the CRM geometry with 3.00deg LoQ aeroelastic wing deflection. Test Case 2a requires a set of seven Medium sized grids on wing geometries with LoQ aeroelastic deflections ranging from 2.75deg to 4.25deg. These were generated by applying the control source setup for the Medium grid from Test Case 1a to the different wing geometries. Similarly, the Medium baseline grid for Test Case 6 was generated on the undeformed (NoQ) geometry.

Using DLR's standard best practice settings concerning the size distribution between leading and trailing edge a Fine mesh (F) for Test Case 1a was setup as a starting point. By adjusting the global source scaling of that mesh, it was sized to meet the given point number from the gridding guidelines. Based on this initial surface mesh all other family members are created by scaling all sources for controlling mesh density by the factor (L+2)/(L+1) specified in the gridding guidelines.

The basic procedure for generating the meshes starts with the quad-dominant surface mesh generation. Anisotropic quadrilateral elements allow the discretization of single curvature surfaces, such as wing leading edges, in an efficient way. A quadrilateral surface mesh allows for elements with higher aspect ratios than triangles, while maintaining or even reducing discretization errors for a given number of mesh points. The amount of triangular surface elements is typically in the order of 0.5% of the total number of surface elements. As examples the Coarse and Fine surface meshes are shown in Fig. 8.

The boundary layer mesh is created by extruding the surface mesh in normal direction to the viscous wall surfaces into the computational domain. Due to the quad-dominant mixed element surface mesh, the advancing layer step is consistently hexahedra-dominant, with some triangle-based prismatic layer stacks where needed. Pyramidal elements are used to achieve a conformal interface between the near-field advancing layer mesh and the farfield advancing-front mesh. The first wall distance Δy_1 is changing with mesh resolution level, Table 6. The wall normal stretching of the cells remains constant at q=1.2. Because SOLAR determines the maximum number of boundary layers by element height-to-width ratio, the number

of layers also is more or less constant (N_{BL}=52...53, cf. Table 6), Fig. 8. The remaining field volume is filled with tetrahedra. To capture the gradients of the resulting flow, especially possible shocks on the wing upper side, this region around the wing is refined locally. The boundary layer height and upper surface refinement changes between Coarse and Fine grids are illustrated in Fig. 9.

Table 6. Computational grids family generated by DLR for Test Case 1a.

Level	Name	No. Points / 10^6	No. Elements / 10^6	Δy_1 / [μm]	N_{BL}
1	Tiny (T)	11.699	31.589	6.560	53
2	Coarse (C)	25.008	64.335	4.374	53
3	Medium (M)	47.065	130.75	3.280	52
4	Fine (F)	76.508	224.10	2.624	52
5	Extra Fine (X)	118.86	367.93	2.187	52
6	Ultra Fine (U)	164.53	534.17	1.874	53

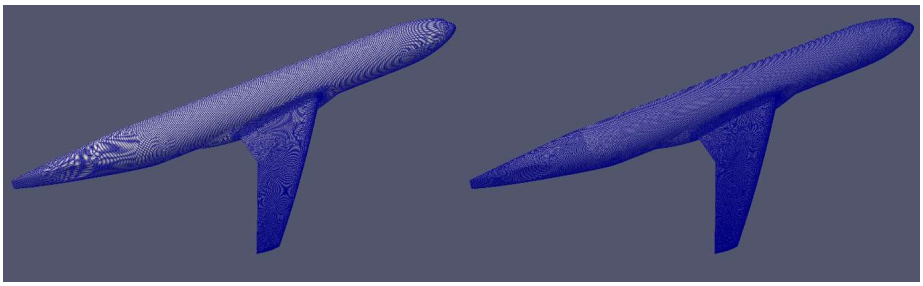

Fig. 8. Surface view for Coarse (left) and Fine (right) meshes at 3.00deg aeroelastic deformation.

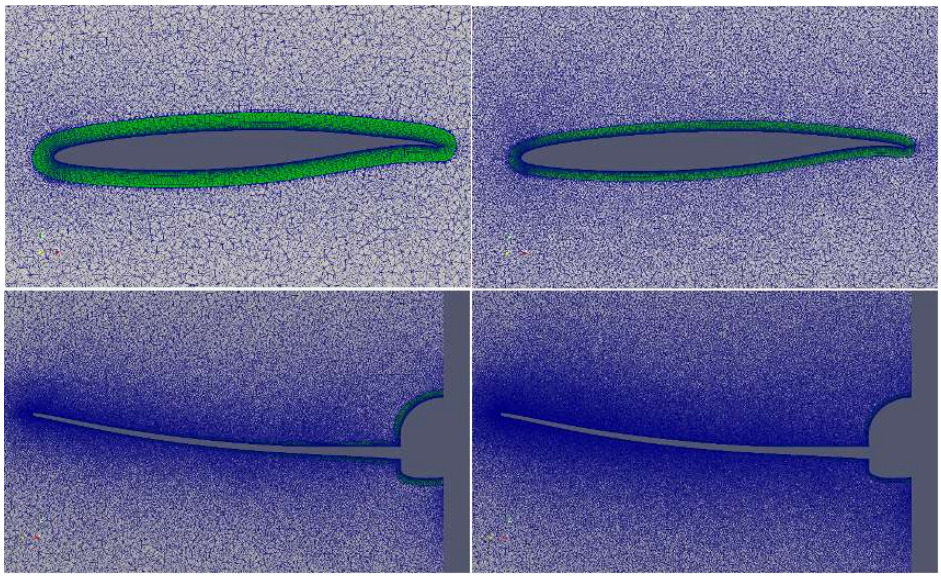

Fig. 9. Boundary layer height of Coarse (left) and Fine (right) meshes and Refined tetrahedra mesh on upper wing for Coarse (left) and Fine (right) meshes.

SOLAR is used in a semi-automated mode, where the geometry of the configuration is subdivided in several zones of either lifting surfaces or bodies. Based on this subdivision, a set of volume sources is automatically distributed over each component. The primary aim is to establish structured areas with hexahedral elements on as much of the surface as possible, for example along the leading and trailing edges of the wing. Secondly, in highly curved regions, like wing leading edges, anisotropy is used in the direction where the flow gradients are small (e.g., in spanwise direction) to reduce the overall number of points. On the leading edges a maximum cell aspect ratio of about 20 was reached in spanwise direction.

IV. Test Case Descriptions

It is recognized that many of the DPW participants are from industry and academia and may have limited time and resources to devote to this type of study. The test case specifications, as with the grid definitions, are set to encourage participation by restricting the number of cases to a manageable number while also providing a challenge to test the state of the art in CFD prediction capabilities. Six test cases were specified for the Seventh AIAA CFD Drag Prediction Workshop, of which, three were optional.

1. **Grid Convergence Study:** Use at least 4 grids of the 6-member baseline grid family for this study. - Preferably, we would like Participants to use all 6 members of the Family. Use 3.00-deg LoQ AE CRM geometry.

   Case 1a. Re = 20M (Required): Flow conditions are: M = 0.85; Re = 20 million; fixed CL = 0.58 +/- 0.0001; Reference temperature = -250°F; 3.00-deg LoQ AE CRM geometry. Grid convergence study on Baseline LoQ Re30 grids.

   Case 1b. Re = 5M (Optional): Flow conditions are: M = 0.85; Re = 5 million; fixed CL = 0.58 +/- 0.0001; Reference temperature = 100°F; 3.00-deg LoQ AE CRM geometry. Grid convergence study on Baseline LoQ Re5 grids.

2. **Alpha Sweep:** Angle-of-attack sweeps will be conducted at two Reynolds numbers using the LoQ aero-elastic deflections measured in the ETW Wind Tunnel Test. Flow conditions are:

   Case 2a. Re = 20M (Required): M = 0.85; Re = 20 million, Reference temperature = -250°F. Use Baseline LoQ Re30 grids.

   Case 2b. Re=5M (Optional): M = 0.85, Re = 5 million, Reference temperature = 100° F. Use Baseline LoQ Re5 grids.

   Angle-of-attack sweep = [2.50, 2.75, 3.00, 3.25, 3.50, 3.75, 4.00, 4.25] degrees. The Medium Baseline grids defined for each angle-of-attack [each solution will use the grid specified for the angle-of-attack] are to be used.

3. **Reynolds Number Sweep at Constant CL (Required):** Flow conditions are: M = 0.85, CL = 0.50, medium grids;

   - Re = 5M, LoQ – Re5 grid using 2.50-deg LoQ AE CRM geometry, Reference temperature = 100° F (Same LoQ Re5 medium grid solution from Case 2b)
   - Re=20M, LoQ – Re30 grid using 2.50-deg LoQ AE CRM geometry, Reference temperature = -250° F (Same LoQ Re30 medium grid solution from Case 2a)
   - Re=20M, HiQ – Re30 grid using 2.50-deg HiQ AE CRM geometry and Re30 grid, Reference temperature = -182° F
   - Re=30M, HiQ – Re30 grid using 2.50-deg HiQ AE CRM geometry and Re30 grid, Reference temperature = -250° F

4. **Grid Adaptation – Alpha Sweep [Optional]:** Angle-of-attack sweep for the CRM Wing-Body using an adapted grid family provided by the participant. Flow conditions are: M = 0.85; Re = 20 million; Reference temperature = -250°F Start the adaptation process from the appropriate Baseline LoQ mesh or aeroelastic geometry. Additional cases can be run for Re = 5 million; Reference temperature = 100°F.

   Angle-of-attack sweep = [2.50, 2.75, 3.00, 3.25, 3.50, 3.75, 4.00, 4.25] degrees. Participants are to document the adaptation process.

5. **Beyond RANS [Optional**]: Solution technologies beyond steady RANS such as URANS, DDES, WMLES, Lattice Boltzmann, etc. Flow conditions are: M = 0.85; Re = 20 million; Reference temperature = -250°F. Single solution at CL = 0.58 or alpha sweep.

   Angle-of-attack sweep = [2.50, 2.75, 3.00, 3.25, 3.50, 3.75, 4.00, 4.25] degrees.

6. **Coupled Aero-Structural Simulation [Optional]:** Flow conditions are: M = 0.85; Re = 20 million; Reference temperature = -250°F. Use the Medium Baseline NoQ Re=30M grid. Single solution at CL = 0.58 and/or an alpha sweep, coupled with computational structural analysis. Static aeroelastic deflections calculated starting from the undeformed NoQ geometry.

   https://commonresearchmodel.larc.nasa.gov/geometry/dpw6-geometries/ accessed 21 February 2023.

   A structural FEM and modal shapes are also available on the CRM Website.

   https://commonresearchmodel.larc.nasa.gov/fem-file/ accessed 21 February 2023.

   Undeflected NoQ geometry/grids for NTF Wind Tunnel Model WITHOUT Nacelle/Pylon and tail to be used as a starting point.

All CRM simulations are to be "free air" with no wind tunnel walls or support system. The boundary layer is to be modeled as "fully turbulent" for all cases. No free or fixed laminar to turbulent transition is to be specified. All cases will use the provided deflected geometries/grids for low dynamic pressure test conditions. A chord Reynolds number of 20 million is specified with a chord Reynolds number of 5 million as optional. Case 3 requires additional solutions at a chord Reynolds number of 20 million and 30 million using the provided deflected geometries/grids for high dynamic pressure test conditions.

To collect a consistent set of data from each participant, template datasets were supplied. These templates request lift, drag (broken down into skin friction and pressure components), pitching moment, pressure distributions at specified span stations, trailing-edge separation locations, dimensions of the side-of-body separation bubble, grid family and sizes, turbulence model, computing platform and code performance, number of processors used, number of iterations required, etc. For Case 6, values of the calculated wing twist and bending deflections were also requested. These workshops capture an extensive amount of information that serves as a snapshot of the industry capabilities of the time. For example, in the seven workshops held thus far, one obvious trend is that the grid size has grown dramatically. The average size of the medium WB meshes in DPW-I through DPW-IV have been 3.2, 5.4, 7.8 and 10.9 million, respectively. This represents a growth rate of ~17% per year during the eight years between DPW-I and DPW-IV. For DPW-VI, this number had grown from 25 to 50 million points for the various families of grids available. A further increase was seen for DPW-VII. The finest level grids have increased steadily, from just over 3 million solution points in DPW-I to 225 million for the in DPW-VII.

V. Results

The level of participation in DPW-VII was excellent by many counts. Users submitted data from a wide variety of sources, code types, grid types, and turbulence models. Some performed studies that specifically addressed the effects of gridding and/or turbulence modeling with the same code. As mentioned above, the geometry, test cases, and data format were all uniformly controlled to facilitate the analysis.

A. Participant Descriptions

The Drag Prediction Workshop is open to any individual, group or organization that wishes to perform the calculations according to the specifications set out by the organizing committee. The response for DPW-VII has decreased somewhat from the previous workshop.

A total of 34 datasets were submitted from 18 different teams or organizations. Of these teams, broken down by location and type as follows:

- 7 North America, 7 Europe, 4 Asia
- 7 Government, 3 Industry, 4 Academia, 4 Commercial

The presentations by each participant will be found at the DPW-VII website [86] and contain a description of the computational method used and results presented. For the Cases the grid type and turbulence model breakdown included:

- **Grid Types:**
  - 4 Overset (3 Teams)
  - 8 Structured Multiblock (5 Teams)
  - 21 Unstructured (12 Teams)
  - 1 Custom Cartesian (1 Teams)

- **Turbulence Models:**
  - 7 SA (many variants)
  - 16 SA-QCR (many variants)
  - 5 SST (many variants)
  - 3 EARSM
  - 1 RSM-ω
  - 1 SSG/LRR
  - 1 AMM-QCR

All participants were asked to submit forces, moments, pressure, and separation data in the standard format. The large number of datasets poses a challenge in the presentation of the data. Each dataset is assigned an alphanumeric (including Greek) symbol type while colors are used to denote grid or turbulence model type depending on context. All the force/moment and pressure plots below follow the scheme listed in Table 7.

Table. 7 DPW-VII Participants

ID	Sym	Name	Organization	Method	Turbulence Model	Grid Type
A1	A	Mitsuhiro Murayan	JAXA	TAS	SA-noft2-R-QCR2000(Crot=1.0)	CommonHybrid
B1	B	Sansica	JAXA	FaSTAR	SA-R-QCR2000	CommonHybrid
B2	b	Sansica			SA-R	
B3	β	Abe, Hiroyuki			AMM-QCRcorner	
C1	C	David Hue	ONERA	elsA	SA-QCR2000	Block-structured grid
C2	c				kwSST-QCR2000	
D1	D	Ben Rider	Boeing	Overflow v2.3e	SA-RC-QCR2000	Overset
E1	E	Dmitry Kamenetsky	Boeing	GGNS-T1	SA	EPIC
E2	e				SA-QCR2000	
E3	E				SA-RC-QCR2000	
F1	F	Rooij, van, Michel	NLR	ENSOLV	EARSMCust	Block-structured grid
F2	f				SST	
G1	G	Krishna Zore	ANSYS	Ansys Fluent	SST-2003	CommonHybrid
G2	g				EARSM	
H1	H	Eliasson, Peter	SAAB/VZLU/FOI	M-Edge	EARSM	CommonHybrid
H2	h				SA	Boeing common multiblock
H3	η				SA	CommonHybrid
I1	1	Frederic Plante, Eric Laurendeau	Polytechnique Montreal	CHAMPS	SA	Overset
I2	i				SA-QCR2000	
J1	J	Thomas Fitzgibbon	FlexCompute	Flow360	SA	CommonHybrid
J2	j				SA-QCR2000	
J3	φ				SA-RC-QCR2000	
J4	Ω				kwSST	
K1	K	Potturi, Amarnatha	Metacomp	CFD++20.1	SARC-QCR	CommonHybrid
L1	L	Shoemake, Lawton	University of Teennesse - Knoxville	Overflow	SA-neg-noft2-RC-QCR	Overset
M1	M	Darbyshire, Oliver	Zenotech	zCFD	SA-neg-noft2	CommonHybrid
N1	N	Pomeroy, Brent	NASA Langley Research Center	Kestrel 12.1	SA-RC QCR	CommJAXACart
P1	P			USM3	SA-R-QCR2000	CommonHybrid
O1	O	Yalu Zhu	Nanjing Xfluids Aerospace Technology Ltd	ASOP	SA-noft2-QCR2013-V	Block-structured grid
Q1	Q	Friedewald, Diliana	DLR (Institute of Aeroelasticity)	TAU	SSG/LRR-ln-omega	CommonHybrid
Q2	q				SA-QCR	
R1	R	Keye, Stefan	DLR	TAU	RSM-ln(w)	CommonHybrid
S1	S	Yannick Hoarau	U-Strasbourg	USMB	SA-QCR	Block-structured grid
S2	s				SST	

B. Case 1: Grid Convergence Study:

This consisted of a grid refinement study at M=0.85, C_L=0.58, and Chord Re=20 million. As an option, a grid refinement study could also be performed at Chord Re=5 million. A standard technique in grid convergence studies is to use Richardson extrapolation [40]. Computational results are plotted versus grid factor, $N^{-2/3}$ (called GRIDFAC in Fig.s), where N is the number of solution points. For second order codes, a linear fit should be observed with decreasing error if the refinement is in the asymptotic region. The y-intercept then estimates the theoretical infinite resolution (continuum) result. The trends with grid factor, broken out by grid type and turbulence model, for total drag of the Wing-Body configuration are shown in Fig. 10 for the required Chord Re=20 million solutions. Overall, with some exceptions, the variation of total

drag with increasing grid size (decreasing grid factor) is very flat. A linear extrapolation of values in the asymptotic region to the theoretical infinite resolution indicates that the bulk of the results converge to a band about 5-10 counts wide! A look at the pressure drag with increasing grid size shows an even tighter grouping for most solutions, Fig. 11. The skin friction drag trend, Fig. 12, is also tight, again with a few exceptions. The variation of pitching moment with increasing grid size is shown in Fig. 13. For many solutions, there is little variation in pitching moment with increasing grid size while for others there was, but even these appeared to be trending to a similar continuum level as the other solutions. The optional solutions for Chord Re=5 million, abet with fewer solutions, show similar characterizes. The trends with grid factor, broken out by grid type and turbulence model, for total drag of the Wing-Body configuration are shown in Fig. 14 for the optional Chord Re=5 million solutions.

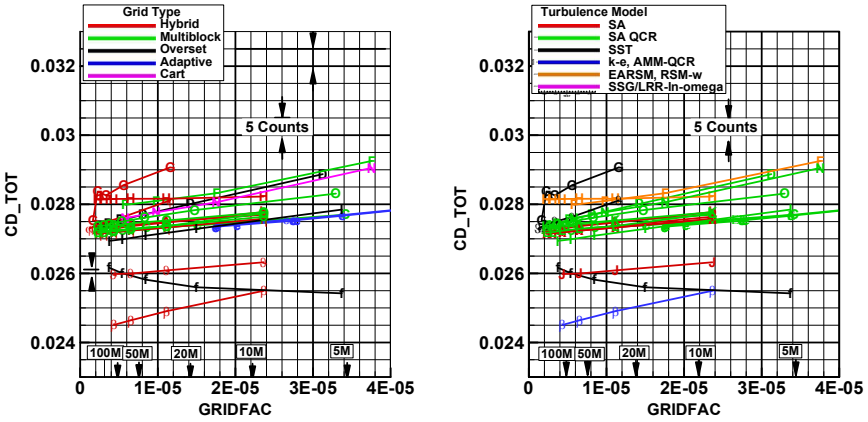

Fig. 10. Case 1a: Total drag by grid type and turbulence model, M=0.85, CL=0.58, Re=20 million.

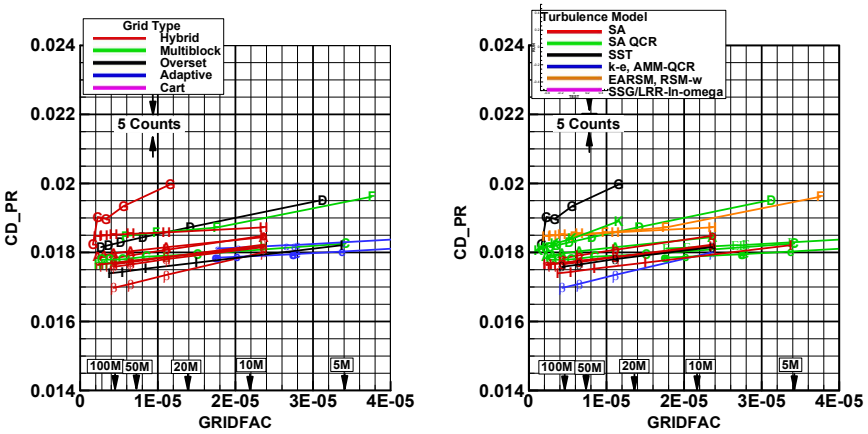

Fig. 11. Case 1a: Pressure drag by grid type and turbulence model, M=0.85, CL=0.58, Re=20 million.

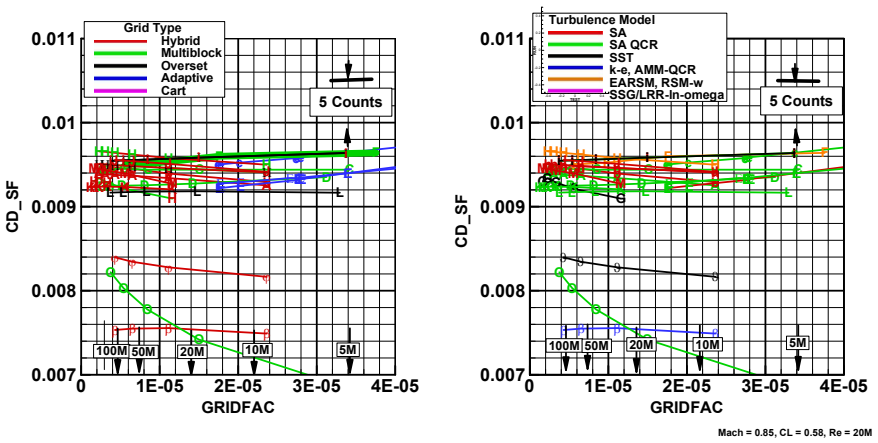

Fig. 12. Case 1a: Skin friction drag by grid type and turbulence model, M=0.85, CL=0.58, Re=20 million.

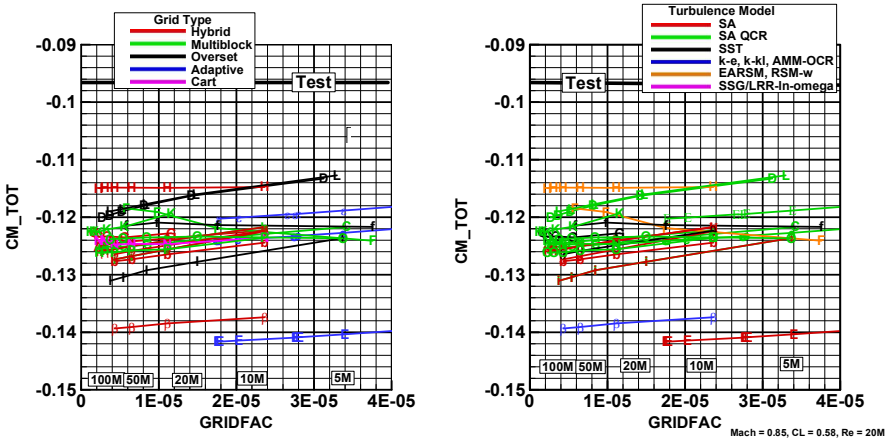

Fig. 13. Case 1a: Pitching moment by grid type and turbulence model, M=0.85, CL=0.58, Re=20 million.

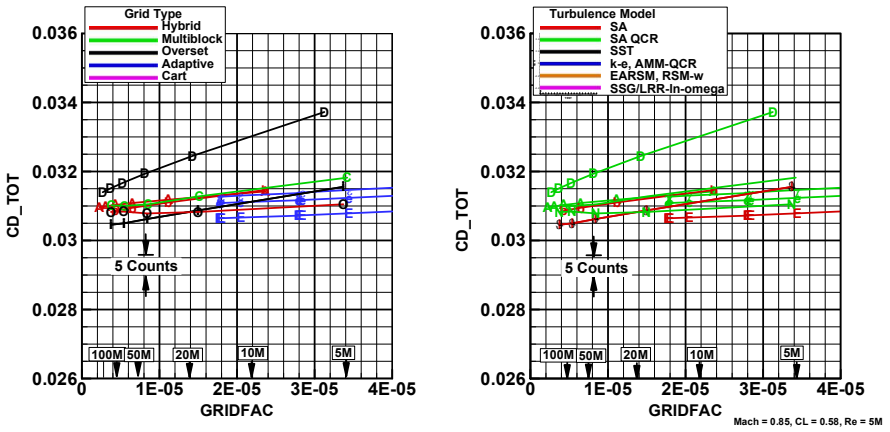

Fig. 14. Case 1b: Total drag by grid type and turbulence model, M=0.85, CL=0.58, Re=5 million.

Figures 15 and 16 show convergence rate, dCDT/dGRIDFAC, and the drag at infinite resolution for the Chord Re=20 million solutions. These values are shown for each data entry and are ordered by drag at infinite resolutions. Results are identified by the alphanumeric symbol assigned to each data entry and by the turbulence model used (Table 2) in Fig. 15 or by grid type in Fig, 16. Not counting the minimum and maximum solutions shown, the average value of the total drag of the Wing-Body CRM is 271.9 counts with a standard deviation of +/- 5.1 counts. This compares with the NTF t215 wind tunnel test value of 284.6 +/- 1.7 counts. Please, be aware that these values should not match exactly due to the different aspects mentioned in previous sections. In addition to other wind tunnel anomalies not modeled in the CFD, the wind tunnel data have not been corrected for the effects of the mounting system! Note that most of the solutions using some form of Spalart-Allmaras turbulence model fell with-in this range. Of these solutions a few showed a convergence rate significantly higher than the norm. Is this due to characteristics of the solver, grid, or both? Figures 17 and 18 show convergence rate, dCDT/dGRIDFAC, and the drag at infinite resolution for the Chord Re=5 million solutions. Fewer solutions were available at this Reynolds number.

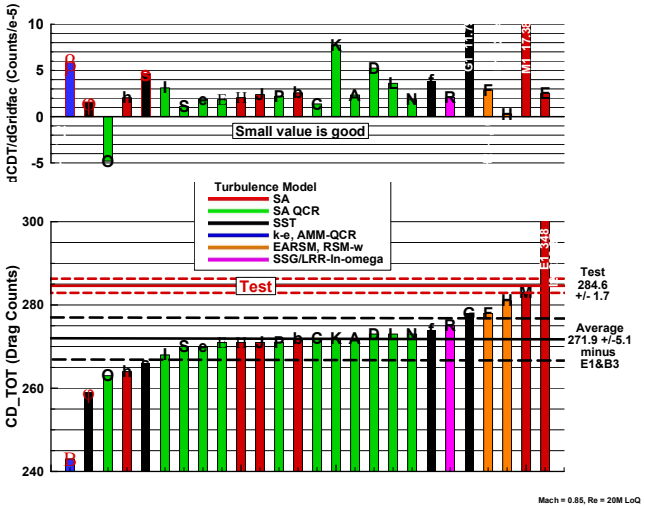

Fig. 15. Case 1a: Total Drag Grid Convergence Sensitivity by turbulence model, M=0.85, CL=0.58, Re=20 million.

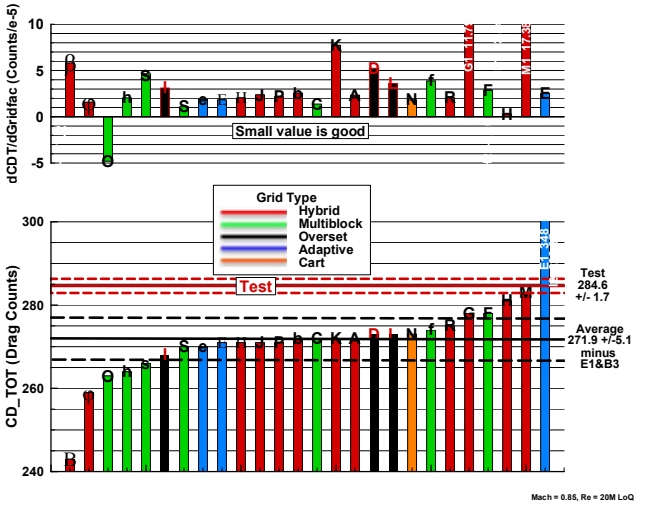

Fig. 16. Case 1a: Total Drag Grid Convergence Sensitivity by grid type, M=0.85, CL=0.58, Re=20 million.

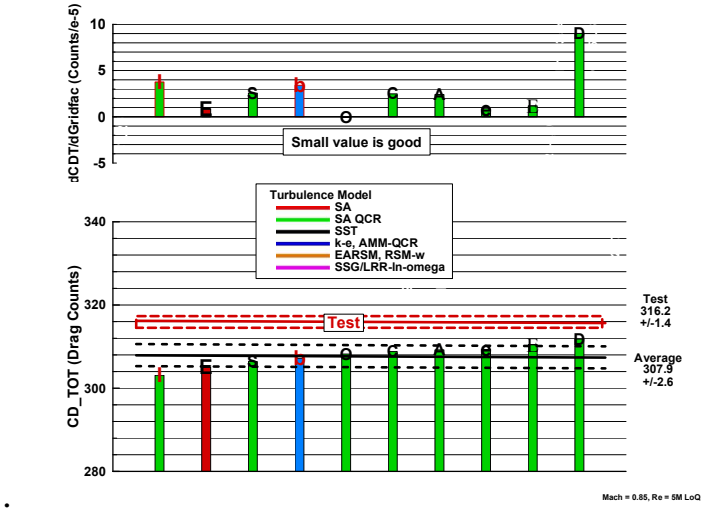

Fig. 17. Case 1b: Total Drag Grid Convergence Sensitivity by turbulence model, M=0.85, CL=0.58, Re=5 million.

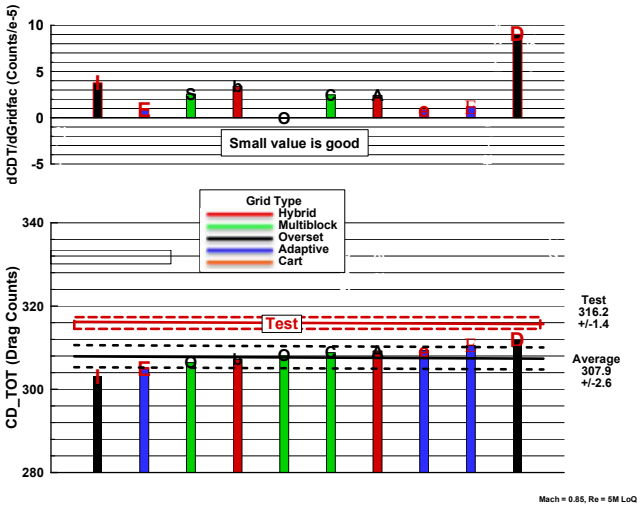

Fig. 18. Case 1b: Total Drag Grid Convergence Sensitivity by grid type, M=0.85, CL=0.58, Re=5 million.

Pressure distributions from the finest grid from each solution set submitted for Case 1a, Chord Re=20 million, are shown in Fig. 19. The lift coefficient chosen for these solutions is near the pitching moment break where shock-induced separation is beginning to have some significant. It should not be too surprising that there is little difference among all the solutions on the inboard part of the wing. The differences that are seen are mainly in the shock location with the differences increasing on the outboard wing stations. Figure 20 shows the pressure distributions for Case 1b with a Chord Re=5 million. Fewer solutions show less scatter in solutions!

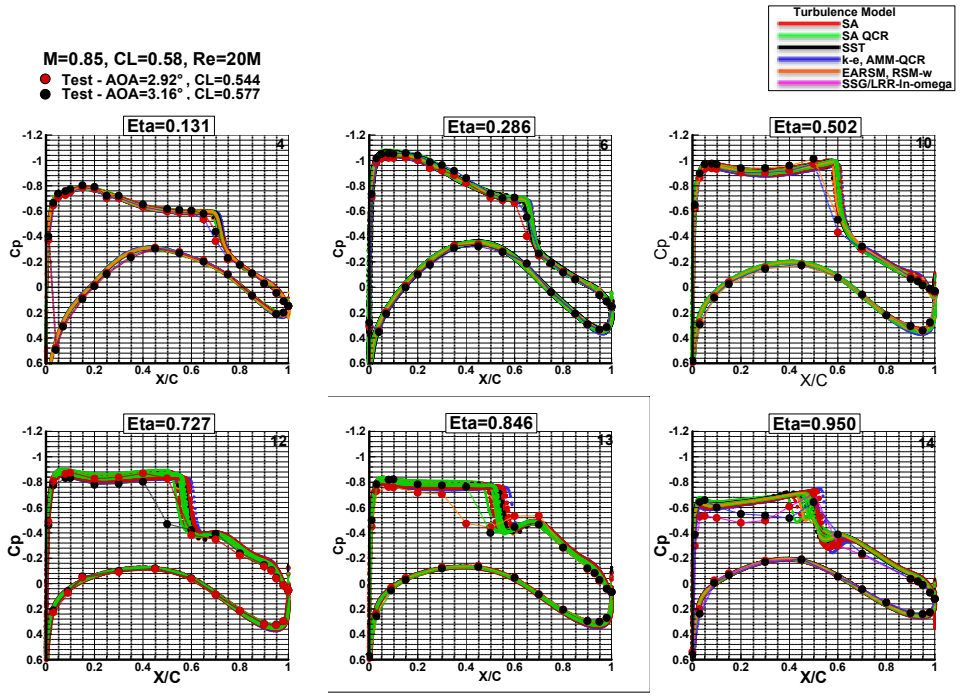

Fig. 19. Case 1a: Wing pressure distributions – All solutions, Finest Grid, M=0.85, CL=0.58, Re=20 million.

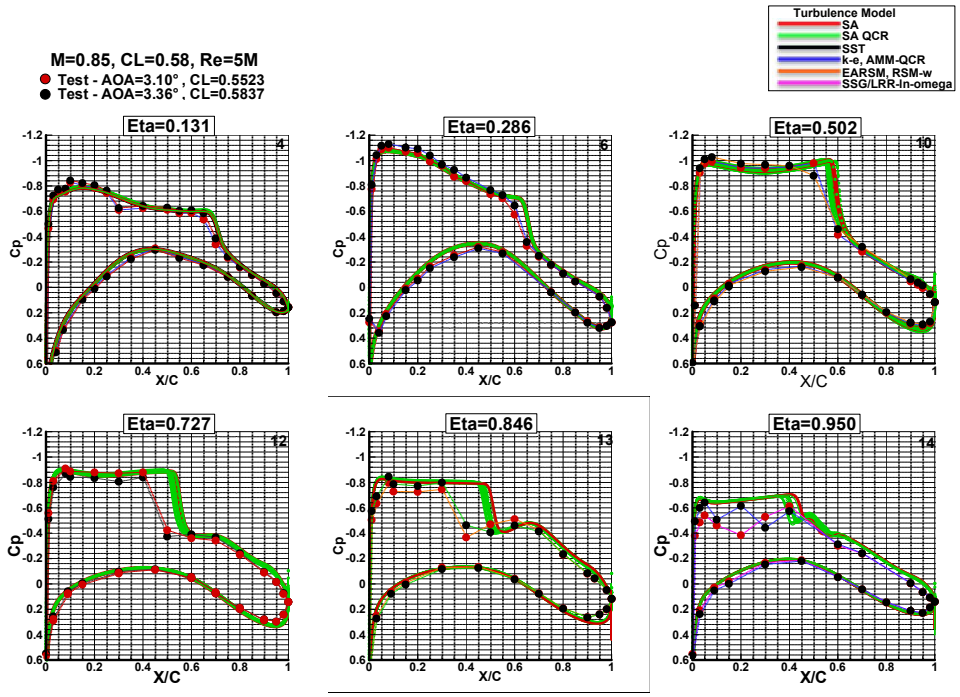

Fig. 20. Case 1b: Wing pressure distributions – All solutions, Finest Grid, M=0.85, CL=0.58, Re=5 million.

Wing section characteristics, lift (normal force) and pitching moment coefficients were requested. These are obtained by integrating the pressure coefficient, Cp, vs. chord fraction, x/c. A Tecplot® Macro script was provided to make these calculations. Unfortunately, the script developed by members of the Drag Prediction Workshop Committee was unable to properly handle some solution formats. Therefore, less than half of the participants have been able to submit these correctly calculated data sets. Wing section characteristics vs. span fraction, eta, are shown for the Case 1a, Chord Re=20 million, in Fig. 21, and Case 1b, Chord Re=5 million, in Fig. 22. It is interesting to note that there is very little difference in the section lift characteristics between the any of the solutions. Furthermore, these show excellent agreement with test data on the inboard part of the wing. This is consistent with the results shown in Figs. 19 and 20 for the pressure distributions. On the outboard part of the wing the computational results show a higher sectional lift than indicated by the test data. These differences are greater for the Chord Re=5 million solutions. These differences will be discussed in more detail in Section VI Issues.

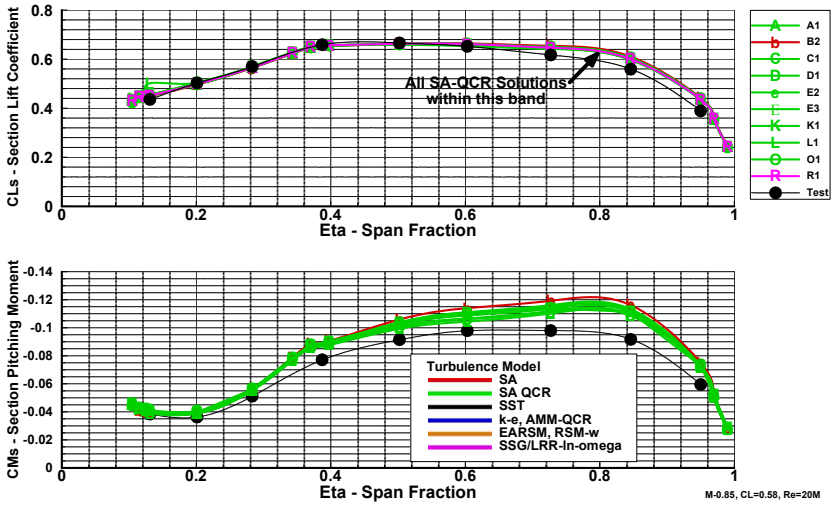

Fig. 21. Case 1a: Wing section lift and pitching moment - all available results – finest grids, M=0.85, CL=0.58, Re=20 million.

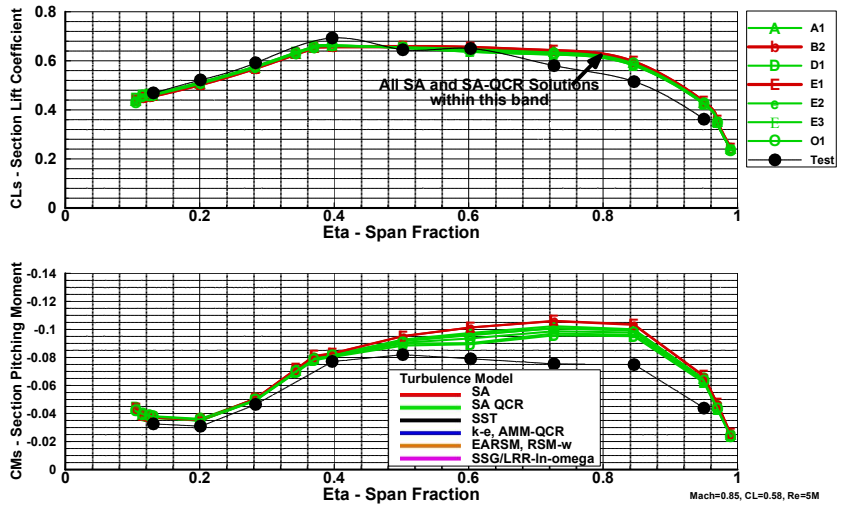

Fig. 22. Case 1b: Wing section lift and pitching moment - all available results – finest grids, M=0.85, CL=0.58, Re=5 million.

The section pitching moment solutions show excellent agreement with test data on the inboard part of the wing. On the outboard part of the wing there is a variation between solutions and a significantly higher section pitching moment compared to the test data. Looking at the pressure distributions in Figs. 19 and 20 shows that the spread in section pitching moment on the outboard part of the wing is due to the spread of the shock location between solutions, and the higher values are due the further aft shock location compared to the test data.

C. Case 2 Alpha Sweep:

The second mandatory CRM case is based on a Wing-Body static aeroelastic/buffet study to investigate the CFD predictions in an angle-of-attack range where significant flow separation is expected. This flight regime is of particular importance to determining aerodynamic loads and stability and control characteristics. Eight angles-of-attack were specified between 2.5° and 4.25° at 0.25° increments. As noted in Section II, in order to account for the static aeroelastic deformation of the wind tunnel model, a separate geometry/grid was defined for each angle-of-attack requested. Computed results of lift, drag, pitching moment, wing section pressure and skin friction coefficients at specified spanwise locations, and locations of flow separation on the wing and body were requested at each angle-of-attack. 29 data sets were provided by the Workshop participants for Case 2a, Chord Re=20 million, and 11 sets for Case 2b, Chord Re=5 million.

Lift and pitching moment results from all the Workshop submittals, along with the NTF and 11-Foot TWT test data are shown in Fig. 23 for Case 2a, Chord Re=20 million. Most of the solutions are clustered within a "fan" that gets progressively wider with increasing angle-of-attack. In general, the solutions are indicating a higher lift at a given angle-of-attack, and a more negative (nose down) pitching moment at a given lift coefficient than indicated by the test data. Some of this level difference could be due to the lack of mounting system corrections to the wind tunnel data. It should also be noted that at the higher angles-of-attack there is a significant amount of buffeting of the wind tunnel model due to the increasing flow separation and shock movement. There is some unsteady content at the higher angles-of-attack that is not represented by the test data, nor simulated by the CFD. The wind tunnel force data are heavily filtered and represent an average value at the flight condition measured. The pressure transducers measuring the wing pressure distributions are not capable of measuring high frequency variations and present average values. Mounting system effects and unsteady aerodynamic content will not account for the significant spread of predicted lift and pitching moment at the lower angles-of-attack where the flow is well attached.

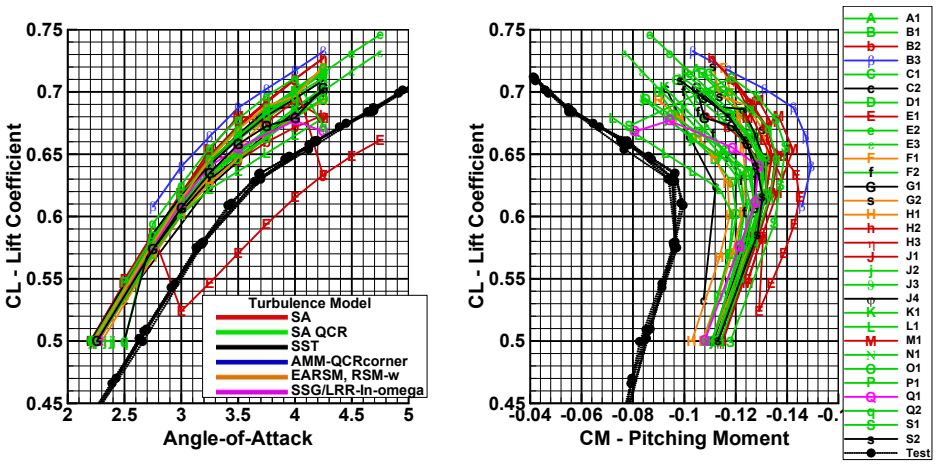

Fig. 23. Lift and pitching moment for all solutions, M=0.85, Re=20 million.

Far fewer outliers were seen in DPW-VII compared to DPW-VI. This was largely due to the reduced use of the SA without QCR turbulence model which is susceptible to premature side-of-body separation as angle-of-attack is increased. The wind tunnel data do not exhibit any evidence of flow separation on the inboard portion of the wing (first row of pressures located at BL=151), nor does it show an early lift break. The

geometrical determination of the side-of-body (SOB) separation bubble requires a manual inspection of surface streamlines. This tedious and somewhat ambiguous task may have discouraged several participants from submitting this information. As such, the resulting separation bubble geometric data is a subset of all submitted solutions. The data that was submitted is shown in Fig. 24 and is grouped according to turbulence model, which showed the strongest correlation to separation bubble width. The limited data set clearly shows that the use of QCR suppresses the rapid expansion of the separation bubble. All of the solutions identified with a separation bubble size greater than BL=151 also exhibited a lift break at or below 4° angle-of-attack and have been identified as outliers.

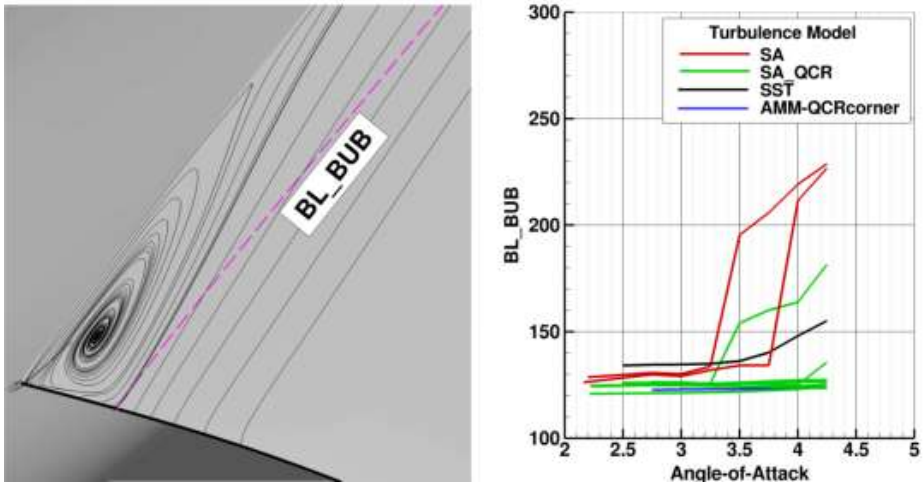

Fig. 24. Side-of-Body Separation for all solutions, M=0.85, Re=20 million.

Pressure distributions at select wing eta stations at angles-of-attack of 4.0°, and 4.25° are shown in Figs. 25 and 26. Several solutions exhibited a large side-of-body separation bubble with increasing angle-of-attack whose effects could be seen in the wing pressure distributions, and in the force and moment data. The wind tunnel data do not exhibit any evidence of flow separation on the inboard portion of the wing (first row of pressures located at BL=151), nor does it show an early lift break. All the solutions identified with a separation bubble size greater than BL=151 (as seen in the pressure distributions or surface streamlines) also exhibited a lift break at or below 4° angle-of-attack and have been identified as outliers. Also evident in the pressure distributions is the large spread of the shock location on the outboard part of the wing. This spread in computed shock location is largely responsible for the fanning out of the lift and pitching moment solutions as angle-of-attack is increased.

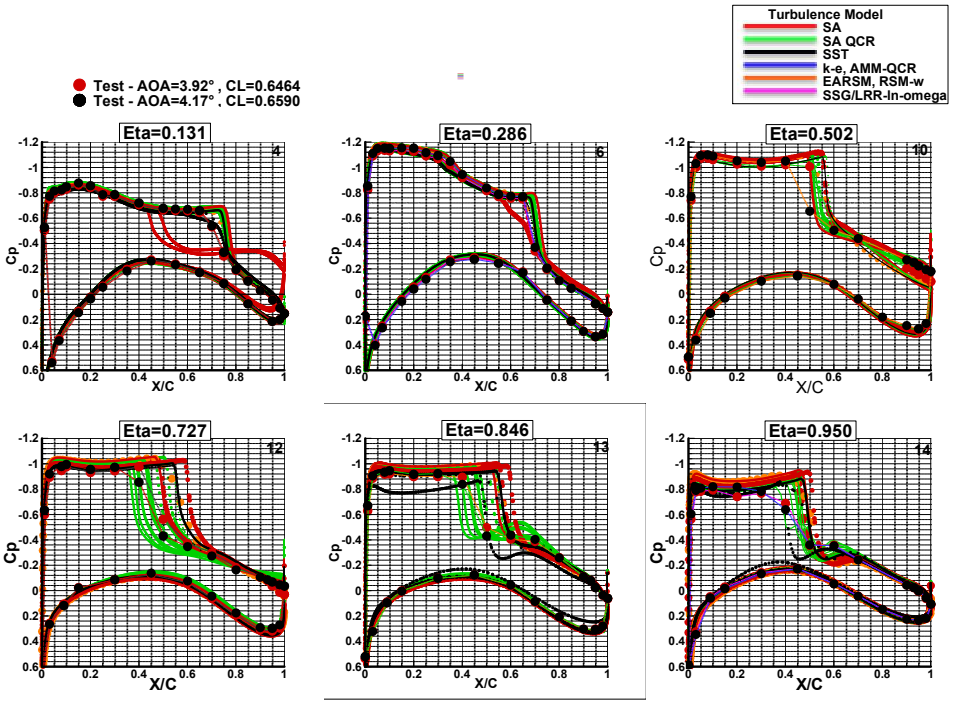

Fig. 25 Pressure Distributions – 4.0° angle-of-attack, M=0.85, Re=20million.

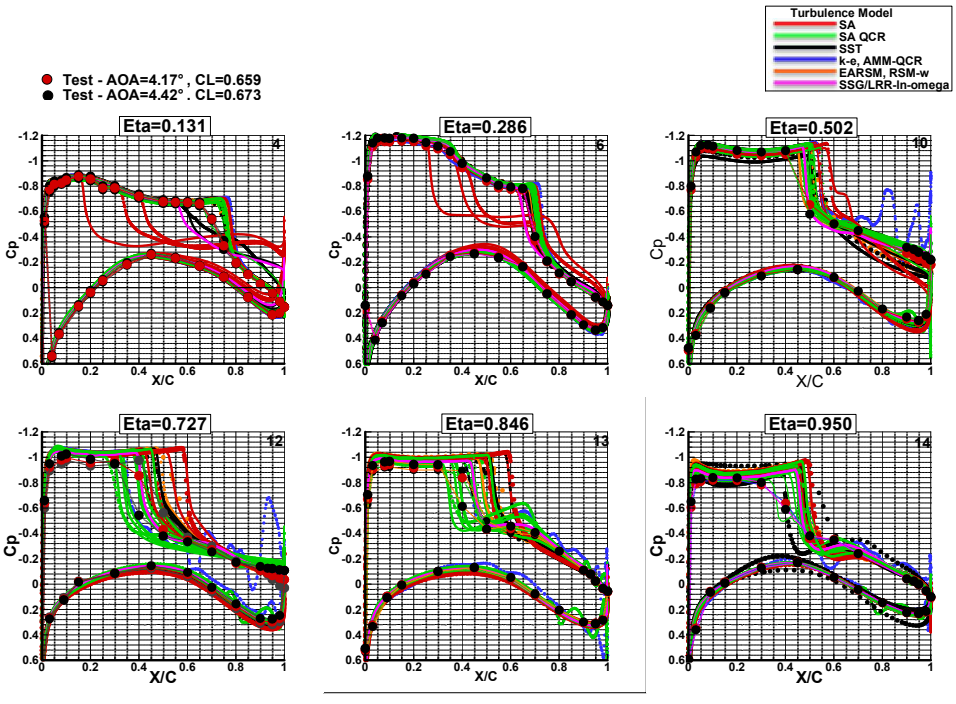

Fig. 26 Pressure Distributions – 4.25° angle-of-attack, M=0.85, Re=20 million.

The drag characteristics of the remaining solutions are shown in Fig. 27. Also shown are test results from three repeat runs at both the NTF and 11-Foot TWT wind tunnels. The drag characteristics are plotted in terms of the idealized profile drag defined as:

$$C_{DP} = C_D - C_L^2/(\pi\ AR)$$

Plotting C_{DP} instead of C_D can be very useful as its variation with C_L is significantly diminished, and therefore, the scale of the plot can be greatly increased. The spread of the drag values is largely driven by the increasing spread of lift with increasing angle-of-attack.

Lift, drag, and pitching moment characterizes for Case 2b, Chord Re=5 million, shown in Figs. 28 and 29, are like those of Case 2a.

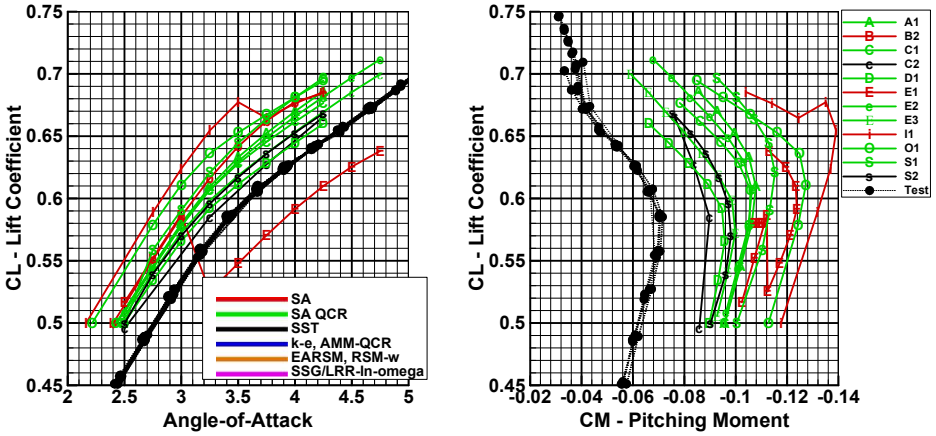

Fig. 28. Lift and pitching moment for all solutions, M=0.85, Re=5 million

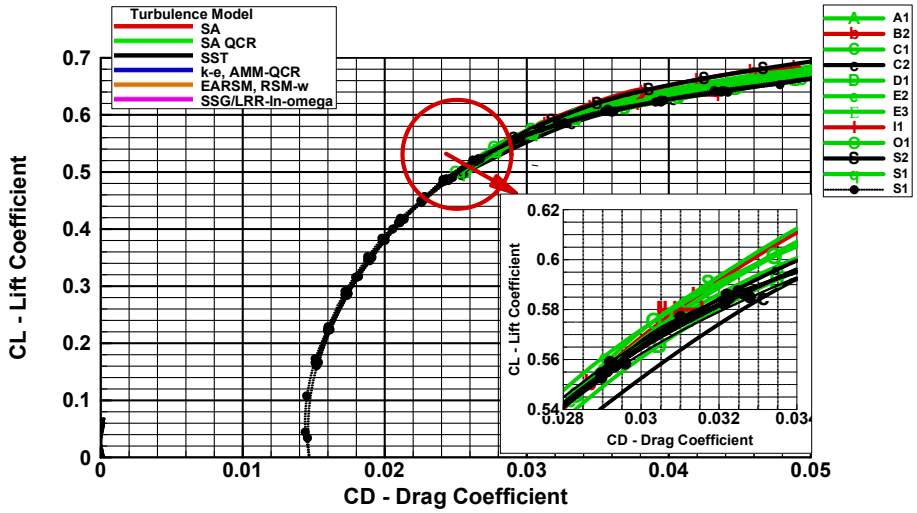

Fig. 29. Idealized Drag, M=0.85, Re=5 million.

D. Case 3: - Reynolds Number Sweep at Constant CL

Case 3 called for a Reynolds number sweep at a constant lift coefficient. For this case the lift coefficient chosen, CL=0.50, is representative of a cruise condition. Ideally this sweep from Chord Re=5 to 30 million would be done at a constant dynamic pressure as well at the constant lift coefficient. Unfortunately, the limitations of the cryogenic wind tunnels prevent this. Instead, Chord Re=5 and 20 million conditions were run at a "low" dynamic pressure, and Chord Re=20 and 30 million conditions were run at a "high" dynamic

pressure. This allows the separation of Reynolds number effects and dynamic pressure (static aeroelastic) effects. Participants were provided with geometries and grids appropriate for those conditions.

Reynolds number and dynamic pressure increments are shown in Fig. 30 for the computed and experimental results. The experimental increments are based on data from two campaigns in the NTF for the Wing-Body configuration. In addition, experimental increments are also shown from data taken in the ETW wind tunnel for the Wing-Body-Tail configuration. The presence of the tail should not affect the increments at these conditions. Increments are shown for: Reynolds change at LoQ (~1380 psi) – Chord Re=20 – 5 million; Dynamic pressure change at constant Chord Re=20 million – HiQ (~1980 psi) – LoQ (~1380 psi); Reynolds number change at HiQ (~1980 psi) - Chord Re=30 - 20 million. Computational increments are shown in index order and are colored by turbulence model type. The computation increments are consistent and of the same order as the test increments. There is little difference in choice of turbulence model at benign flight condition. As Case 2 suggests, this will not be the case at more extreme conditions with significant flow separation.

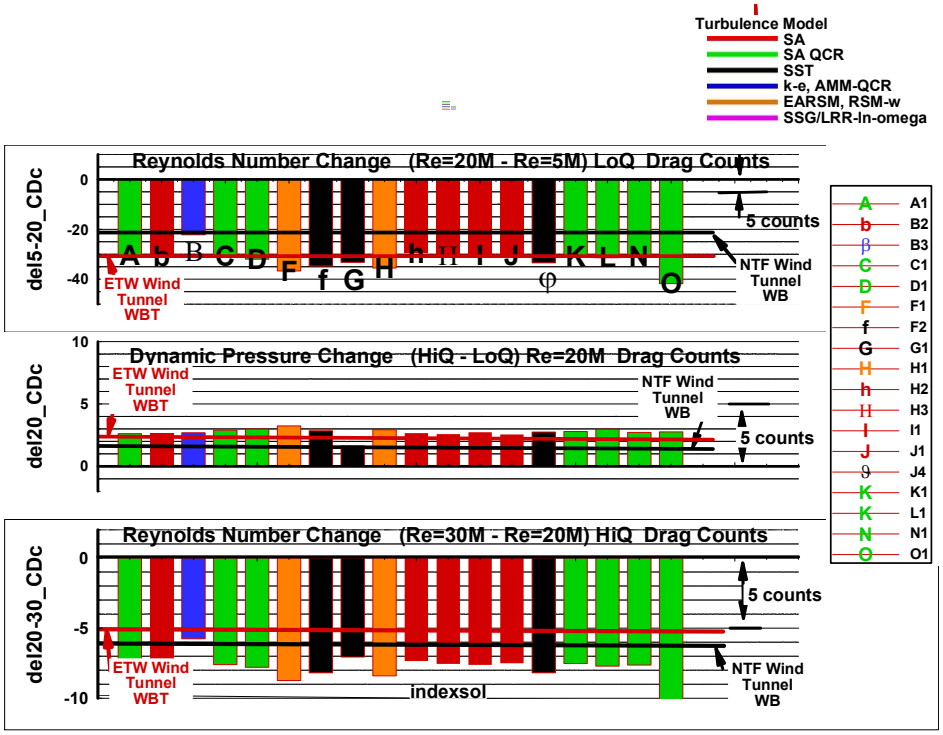

Fig. 30. Reynolds Number Sweep at Constant CL=0.50

E. Case 4: - Grid Adaptation [Optional]

New to DPW-VI was the request for grid adaptation solutions of the CRM Wing-Body configuration as an optional case. A similar request is made in DPW-VII but at a higher fixed lift, C_L=0.58. Unfortunately, only four solution sets were provided by two organizations. Three solutions, E1, E2 and E3, are based on the same solver, using the same adaptation technique, but differed in the version of the Spalart-Allmaras turbulence model. GGNS-TI employs 2nd-order node centered SUPG finite-element discretization with a strong solver that achieves machine precision residual convergence [100]. It employs the EPIC (Edge Primitive Insertion Collapse) adaptive grid tool [101] focusing on a sizing metric derived from the Mach Hessian or Entropy Adjoint error. The adaptive mesh process consists of a sequence of adaptation cycles. Each adaptation cycle consists of running a flow solution to convergence, generating a sizing request for the next grid, generating a new adaptive grid that conforms to the sizing request, and interpolating the solution to the new mesh. The sequence of adaptation cycles is continued until the output of interest reaches convergence. N1, Kestrel [102], employs HLLE++ and LDD+ viscous flux with 2nd

order spatial and temporal accuracy. Initial grids used the committee provided JAXA unstructured/Cartesian grids. Adaptive mesh refinement was performed on the off-body Cartesian grids.

Total drag as a function of the grid factor (GRIDFAC) for the four adapted grid solutions for Chord Re=20 million is shown on the Fig. 31. Note that the GRIDFAC scale has been greatly expanded compared to that shown in Fig. 10 for Case 1. N1 adaption began from the existing coarse grid from Case 1 of about 8.9 million cells and ended up 291 million cells. The E1, E2, and E3 solutions started with a small grid of about 16,000 cells and ended up with about 13.5 million cells after 22 to 24 iterations. Solution E1, using the Spalart-Allmaras (SA) turbulence model (w/o QCR), suffered a massive side-of-body separation on the 10th grid iteration which remained in the subsequent iterations. Solutions E2 (SA-QCR2000) and E3 (SA-RC-QCR2000) adaptive grid solutions converged to the continuum similar to N1 and the fixed grid solutions shown in Figs 15 and 16. Results for Chord Re=5 million submitted by GGNS-T1 did not suffer the large side-of-body separation for solution E1. Solutions E1, E2, and E3 yielded similar results to the fixed grid solution shown in Figs. 17 and 18, but with much smaller grids. The wing pressure distributions from the adaptive solutions are included with the fixed grid solutions shown in Figs. 19 and 20. The adaptive grid solutions tend to have the characteristic of a sharper definition of the shocks.

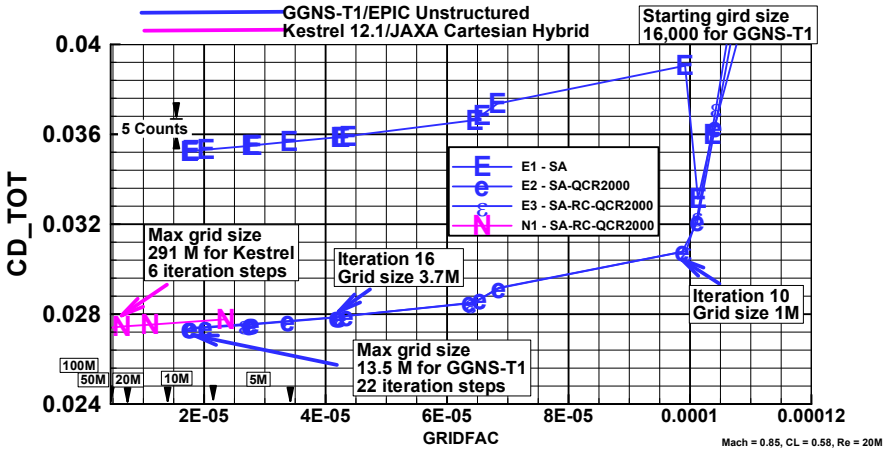

Fig. 31. Case 4: Adapted Grid Total Drag, M=0.85, Re=20 million.

Little benefit is seen for adaptive grid solutions compared to fixed grid solutions for this geometrically simple wing-body geometry. The resultant grids may be smaller, but the work required to obtain these solutions can be several times greater than that required for a fixed grid solution. The promise that solution adaptive grids bring is that they should be able to deliver a consistent set of solutions for configurations, and/or conditions for which prior gridding experience may not be available. Even for this configuration, the "optimum" grid distribution will change dramatically for a drag rise series ranging from Mach = 0.70 to 0.90. Decades have been spent developing and validating gridding guidelines for these "simple" geometries and expected flow features. Additional work remains to be done to bring this technology to a "production" capability for 3-D RANS. It is a technology that needs to be matured.

F. Case 5 - Beyond RANS [Optional]

Solution technologies beyond steady RANS such as URANS, DDES, WMLES, Lattice Boltzmann, etc. were sought for DPW-VII. Unfortunately, insufficient information was available to draw any firm conclusions.

G. Case 6 - CRM WB Coupled Aero-Structural Simulation [Optional]

The purpose of Test Case 6 is to compute a steady aeroelastic equilibrium state for the flow conditions listed in Section 4. Unlike with the other DPW-VII test cases, only the undeformed jig shape geometry of the wing is provided. Here, the flight shape is the result of the coupled simulation. Unfortunately, only two participants have submitted data for this optional case. Therefore, this summary will only consist of a brief comparison of results and not include any statistics.

A common approach to static aeroelastic simulations is sketched in Fig. 32. The simultaneous interaction between the outer flow field and the flexible aircraft structure is simulated in a closed coupling loop. This loop includes solvers for CFD and Computational Structural Mechanics, indicated here as CSM. Coupling between CFD and CSM is implemented through interpolation algorithms for aerodynamic forces and structural deflections. The simulation starts by computing an initial CFD solution on the undeformed mesh and proceeds until convergence is reached.

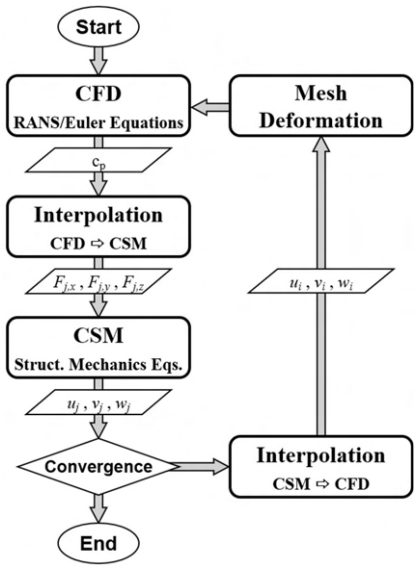

Fig. 32. Example for a Fluid-Structure-Interaction (FSI) simulation procedure.

The method of interpolating aerodynamic forces to the structural domain and performing a static analysis to compute deflections is usually called a *direct* coupling approach. It was used by both participants. Another principal coupling method uses the structure's eigenvectors to approximate static deflections. It requires transforming the structural system to modal space but has the advantage of not needing a (potentially time-consuming) structural solver within the coupling loop. This method is usually referred to as *modal* coupling approach.

Table 8 gives an overview of the methods and software tools used by the participants. Both participants use RANS CFD solvers, a turbulence model, common hybrid grids, and a coupling approach with direct interpolation of forces and deformations. The submitted data sets include wing bending and twist deformations, sectional lift and moment distributions, and static pressure distributions.

Table 8. Overview of aeroelastic simulation methods used for Test Case 6

Organization	Metacomp Technologies Inc., USA	German Aerospace Center (DLR)
ID	K1	R1
CFD Code	CFD++ 20.1	TAU 2020.1.0
Turbulence Model	SARC-QCR	RSM-*ln*(w)
Grid Type	Common Hybrid (JAXA)	Common Hybrid (DLR)
CSM Code	ICSM++	NASTRAN 2019.0
Coupling Method	*direct*	*direct*
Force Interpolation	nearest neighbor	nearest neighbor
Mesh Deformation	RBF	RBF

In Fig. 33 the spanwise bending and twist deformation results from both participants are plotted in comparison to experimental data from the Trans National. Access test campaign at the European Transonic

Wind Tunnel (ETW) in Cologne, Germany [91]. It should be kept in mind that all deformations shown here relate to the wind tunnel model scale which is 2.7% of the full-size CRM. The measured deformation, represented here by black symbols, was also used to derive the aeroelastically pre-deformed wing geometries for the other DPW-VII test cases. The blue line is almost curve fitting the test data, while the red line over-predicts bending by about 10%. For the aerodynamically more relevant twist deformation both participants predict the measured data accurately with less than 0.1% deviation. Both results lie within the measurement accuracy, indicated here by black error bars. Similar results were found for other angles-of-attack.

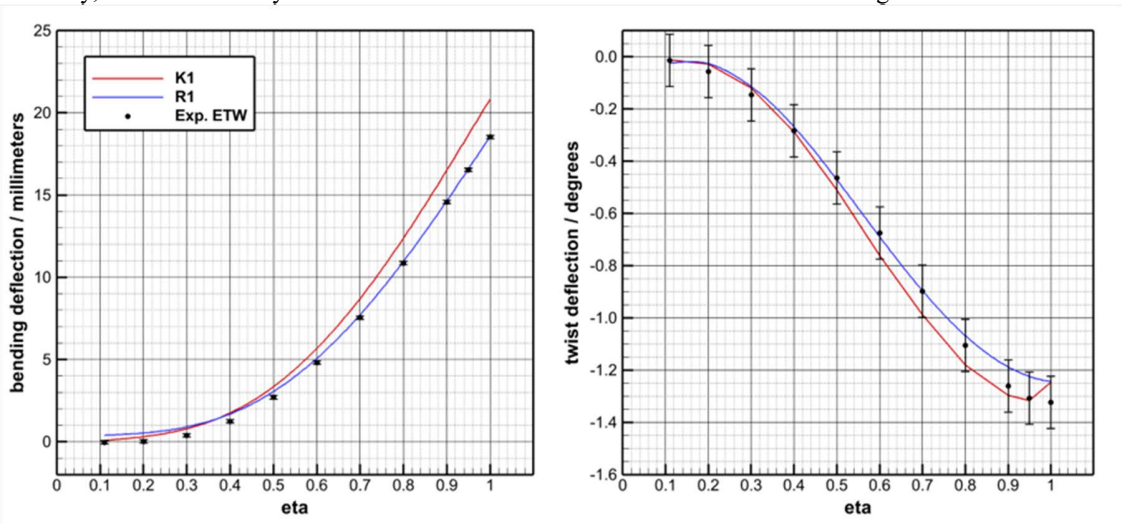

Fig. 33. Wing bending and twist deformations at CL = 0.58.

Figure 34 shows the bending and twist deflections at wing tip, plotted over angle-of-attack. In each graph, the isolated squares to the left represent the target-lift case. Bending results for both participants show an almost constant offset to measured data and between each other. Twist deviations remain small and within the experimental errors over the entire angle-of-attack range. These results demonstrate that both aeroelastic simulation methods are able to correctly predict wing deformations for varying aerodynamic loads.

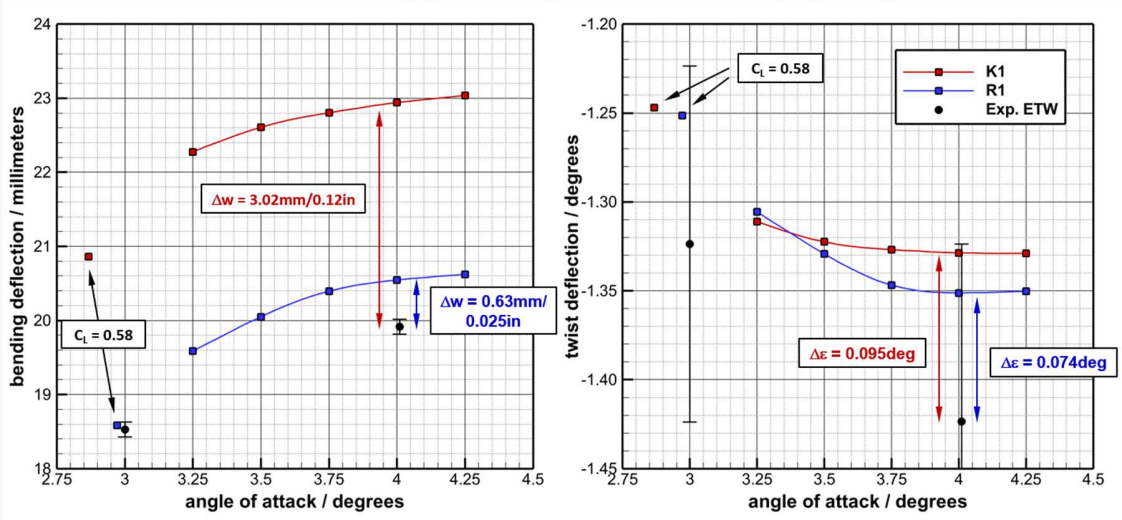

Fig. 34. Bending and twist deflections at wing tip for different angles-of-attack.

The static pressure distributions shown in Fig. 35 were taken from different DPW Test Cases. The green lines are from Case 1, where a fixed, pre-deformed geometry is used, the blue lines represent Case 4 results, where an additional grid adaptation was performed, and the purple lines show the results from the coupled aeroelastic simulation. Apart from some minor differences on the outboard wing, an overall very good agreement between the different simulation methods, and between numerical and experimental data is

observed. These results show that the aeroelastic simulation correctly computes the wing pressure distribution without the need to provide a deformed wing shape.

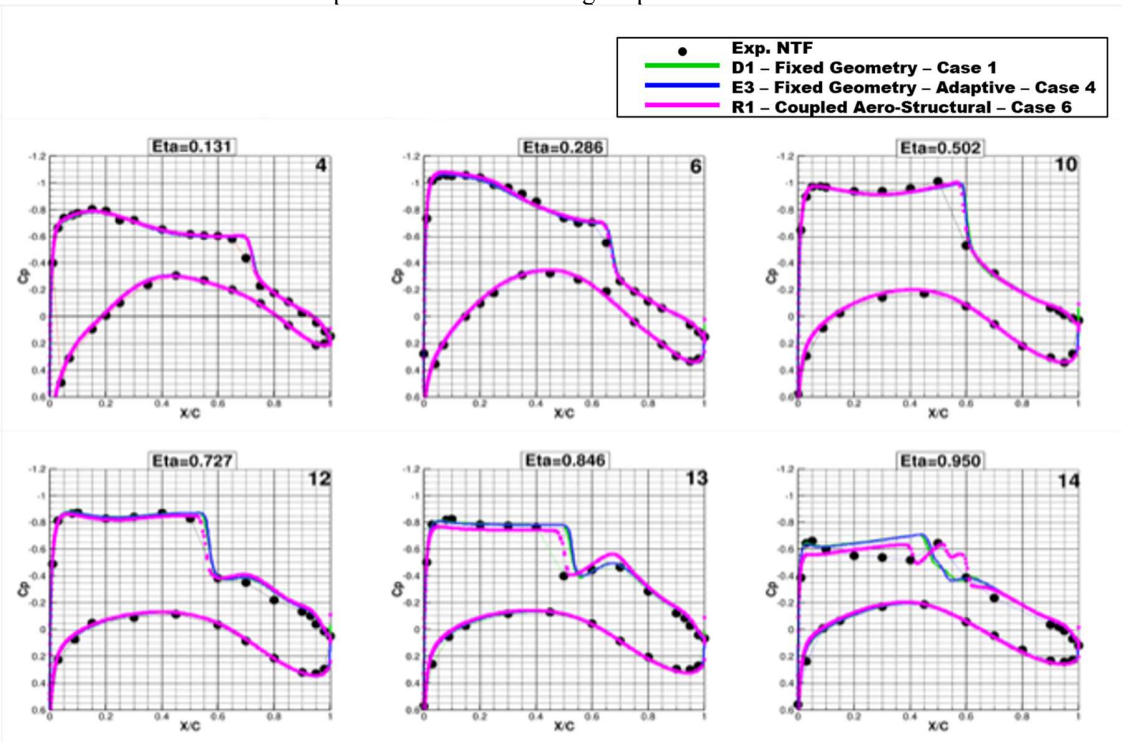

Fig. 35. Comparison of chordwise static pressure distributions for three different test cases and experimental data – M=0.85, Re20M, CL=0.58.

Figure 36 is focusing on the comparison between the two case 6 participants again. In the upper graph sectional lift distribution is plotted over wingspan, the lower row shows chordwise pressure distributions for selected spanwise sections. Despite the very good agreement of pressure distributions between the two participants, there is a quite considerable offset of the red curve with respect to the blue curve and experimental data. Presently, the reason for these discrepancies is unclear and under investigation. It may possibly be related to the integration of static pressure over different underlying surface grid patterns, and not to actual differences between the two simulation methods.

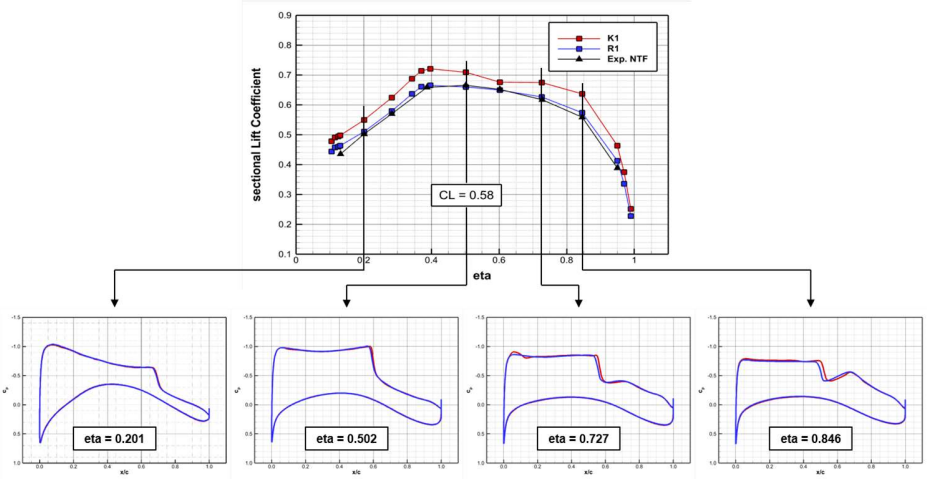

Fig. 36. Comparison of sectional spanwise lift and chordwise static pressure distributions.

Based on the limited amount of data available it is difficult to draw general conclusions for Test Case 6. However, both participant's methods are capable of correctly predicting wing deformations and static pressure distributions under varying aerodynamic loads. As a result, a good agreement is observed between the two participants, and in comparison, to results from other DPW test cases that require pre-deformed wing geometries.

VI. Issues

An important goal of the DPW series of workshops is to identify significant issues/shortfalls in need of further CFD development. DPW-VII highlights continuing issues that, while seeing some progress over the years, continue to plague the state of CFD and experiment. More detailed information about how the experimental data were generated is needed to better validate the CFD, and to provide the detailed information necessary to improve the turbulence models and decide whether unsteady simulations are necessary.

A. Premature Side-of-Body Separation

The prediction of premature side-of-body separation continued to plague some simulations. At the design condition of M=0.85, C_L=0.50, where we can expect little or no flow separation, this is not an issue. However, as angle-of-attack is increased, some solutions did exhibit excessive side-of-body separation as defined as an adverse pressure distribution influence at the first row of pressure taps on the wind tunnel model wing (located at BL=151). As in previous workshops these solutions were using the SA or SST turbulence model. Solutions that avoided premature separation with these turbulence models have typically been using a block structured or overset grids as was the case in this workshop. In addition, in two out of six solutions using the SA or SST turbulence model, the same hybrid grid, but different solvers also avoided premature separation. Experience has shown that premature separation with these turbulence models is very sensitive to gridding details in the wing-body junction region.

The use of the quadratic constitutive relation (QCR) in the SA or SST turbulence model eliminates the premature separation. In addition, two equation turbulence models, the RSM-ln(ω), SSG/LRR-ln-ω. kωSST, kωSST-QCR2000, AMM-QCRcorner and EARSM, turbulence models did not show any evidence of premature SOB separation. Premature side-of-body separation was much less of an issue in DPW-VII than experienced in previous workshops. This type of 3D corner flow separation continues to receive more attention in turbulence model development and CFD application, e.g., the comprehensive NASA Juncture Flow Experiment [103,104].

B. Excessive Aft-Loading

Another ongoing issue can be seen in Figs. 23 and 28 for lift and pitching moment and in Figs. 21 and 22 for wing sectional lift and pitching moment distributions. The lift and pitching moment solutions show a lift higher than experiment and pitching moment more negative than experiment on the outer portion of the wing. This might partially be explained by the lack of corrections to the experimental data for the upper swept sting support to the wind tunnel model. These corrections require a special set of wind tunnel tests using different mounting systems to the model. These tests were not carried out for the CRM in any of the wind tunnel campaigns. Computational studies [89, 94, 95] on the impact of the mounting system show that its effect will be to reduce lift and reduce the nose-down pitching moment. These studies were based on the CRM model with the horizontal tail and therefore, cannot be directly applied this configuration without a tail. The mounting system will have a much greater effect on the model with the horizontal tail than without. In any case, the test corrections would still not explain the spread of values of the computational results at a given angle-of-attack/C_L conditions. However, the wing pressure distributions do offer a clue. Pressure distributions around the wing trailing edge from all the available solutions submitted at the M=0.85, C_L=0.58 and from the comparable test data are shown in Fig. 37. As long as the flow is attached, these distributions vary little over the range of conditions of interest. The pressure coefficient values on the upper surface of the wing are consistently lower (more negative) than those of the test data. Similarly, the values on the lower surface of the wing are consistently higher (more positive) then those of the test data. The difference between the upper and lower surface represents lift and contributes to negative section pitching moment. These differences become more aggressive the further outboard on the wing. This is seen in Figs. 21 and 22 in the spanwise sectional lift and pitching moment characteristic. The CFD sectional data match the experiential data well on the inboard part of the wing but predict higher lift and more negative pitching moment on the outboard part of the wing. This excessive “aft loading” is seen from every turbulence model, gridding

scheme, and solver type presented in this workshop. It is highly unlikely that this excessive "aft loading" is due to experimental issues. The computational results of pressure distribution, and forces and moments, are self-consistent. In the wind tunnel test, the instrumentation is completely independent. The geometry of the wind tunnel model has been validated. The nearly solid nature of the wing minimizes any chordwise aeroelastic effects. Pressure distributions from the Case 6 aerostructural aeroelastic computations are included in Fig. 37. This excessive "aft loading" prediction has also been seen on other wind tunnel models with significant trailing edge camber. While progress has been made with the premature SOB separation, the question of the excessive "aft loading" remains an issue, needs further investigation.

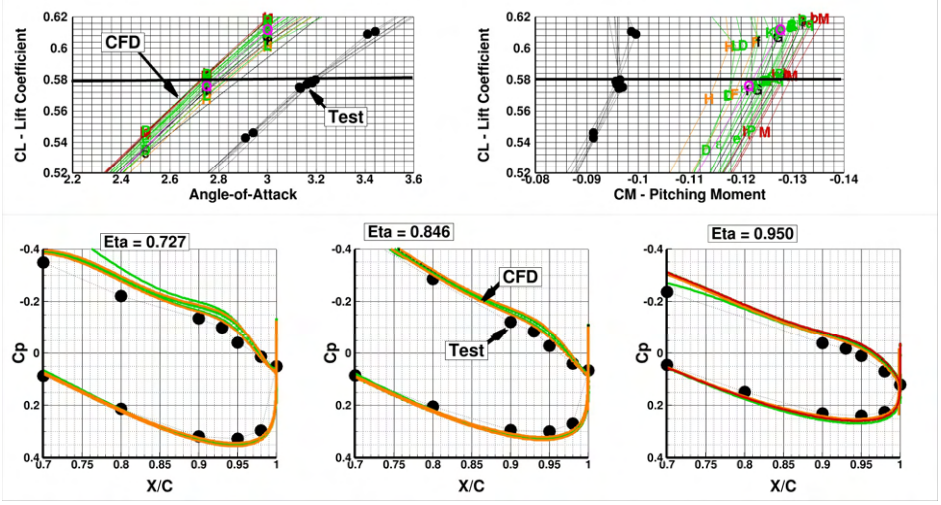

Fig. 37 "Excessive Lift" - Force and Moment and Trailing Edge Wing Pressures at M=0.85, CL=0.58, Re=20 million – All Solutions.

C. Solution Spread

In addition to the "aft-loading" issue, Figs. 23 and 28 also show that the spread in lift at a given angle-of-attack and the spread in the pitching moment at a given lift coefficient increases with increasing angle-of-attack and lift coefficient, respectively. This "spread" is in addition to the level changes caused by the excessive "aft loading." Looking at the wing pressure distributions at the outboard most three wing stations shown in Figs. 19, 25, and 26 provides a clue for the increasing spread. These show pressure distributions for increasing angles-of-attack. As the angle-of-attack is increased so does the spread of shock location at the outboard stations. Figs. 25 and 26 show pressure distributions at 4° and 4.25°angle-of-attack. Note the large variation of shock location from these solutions. Shock location is largely driven by shock-induced separation at this condition. Compare this to the tight spread of shock locations shown in Fig. 19 from all solutions at C_L=0.58, where there is little or no shock-induced separation. Each one of these solutions on its own is a valid solution, yet as angle-of-attack increases so does the spread of shock location on the outboard portion of the wing which is driven by the details of shock-induced separation.

As seen in Fig. 37, in the addition to the bulk shift of angle-of-attack and pitching moment at a constant lift coefficient (excessive aft loading) there is also a smaller variation around that average shift that is be due to the small differences in shock locations at CL=0.58. Analysis (DPW-VI) has shown even smaller variation of pressure distributions and shock location between solutions at CL=0.50. We know that in a well-executed wind tunnel or CFD campaign we can have greater confidence in "deltas" rather than in absolute levels. We can have greater confidence in the variation of lift and pitching moment with the variation with angle-of-attack. By adding a constant value (different for each solution) to angle-of-attack and pitching moment to each solution to match the values of the average of NTF and 11-Foot test data at a CL = 0.53, the CFD solutions can be collapsed around the experimental data as shown in Fig. 38 for Chord Re=20 million, and Fig. 39 for Chord Re=5 million solutions. The value of CL = 0.53 was chosen to encompass all the submitted solutions at a condition where the flow should be free of shock-induced separation. These figures clearly show the variation of lift and pitching with increasing angle-of-attack. Note that the solution spread starts at around CL = 0.61 or between 3.0° and 3.25° angle-of-attack for Re=20M and around CL = 0.58 or between

3.25° and 3.50° angle-of-attack for Re=5M. This represents the beginning of significant shock-induced separation. At 4.25° angle-of-attack, the spread in lift and pitching moment is large. While this approach is somewhat unorthodox, it does allow a better assessment the behavior of lift and pitching moment with increasing angle-of-attack.

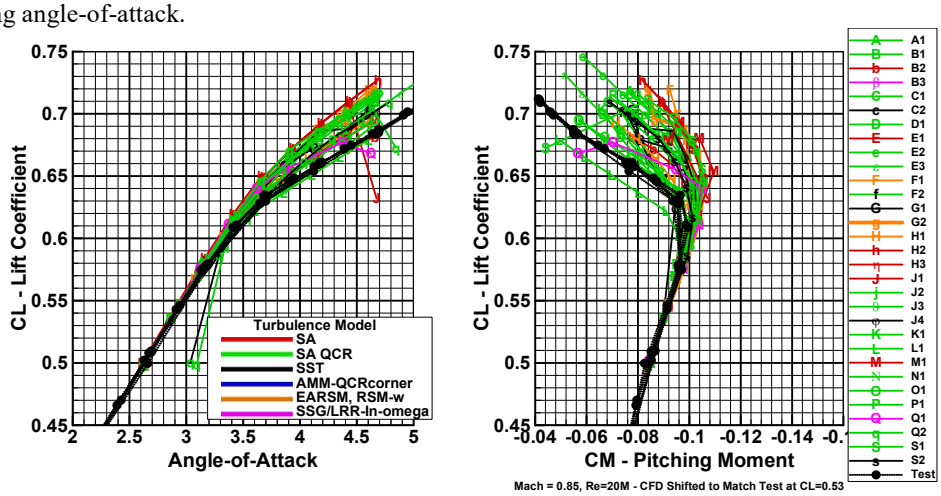

Fig. 38. Lift and Pitching Moment Shifted to Match Experiment at CL = 0.53, Chord Re=20 million.

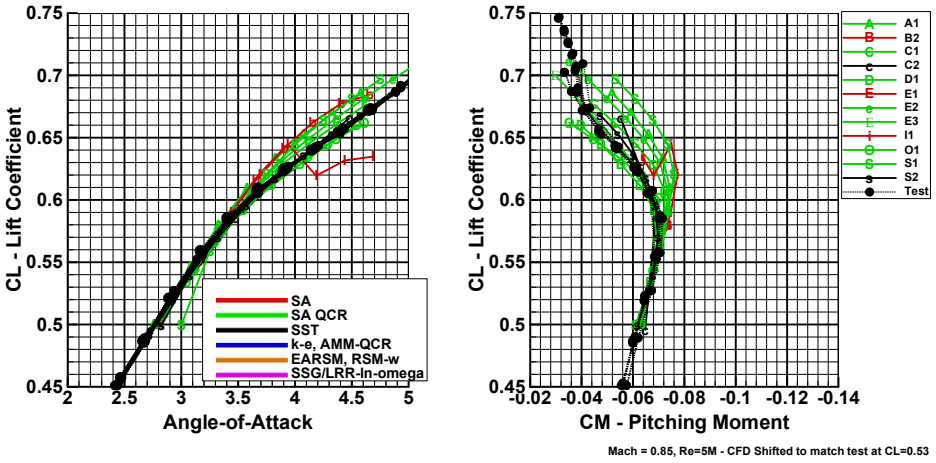

Fig. 39. Lift and Pitching Moment Shifted to Match Experiment at CL = 0.53, Chord Re=5 million.

Eliminating (pruning) solutions that deviate from the test data at the higher lift coefficients leaves a small number of solutions that best match the experimental data, shown in Fig. 40. Also shown in this figure by the dashed lines are the limits of the spread of CFD solutions. For the Case 2a (Chord Re=20 million) only four out of 34 solutions match test data well up until a lift coefficient of 0.65. Two (J3, O1) continued to follow the experimental trend quite well, the other two (D1, E3) started deviating away from the test data. All four solutions used a variation of the SA with QCR turbulence model. Two (D1, O1) used a structured multiblock or Overset grids. The other two (E3, J3) used an unstructured hybrid type grid – see Table 7.

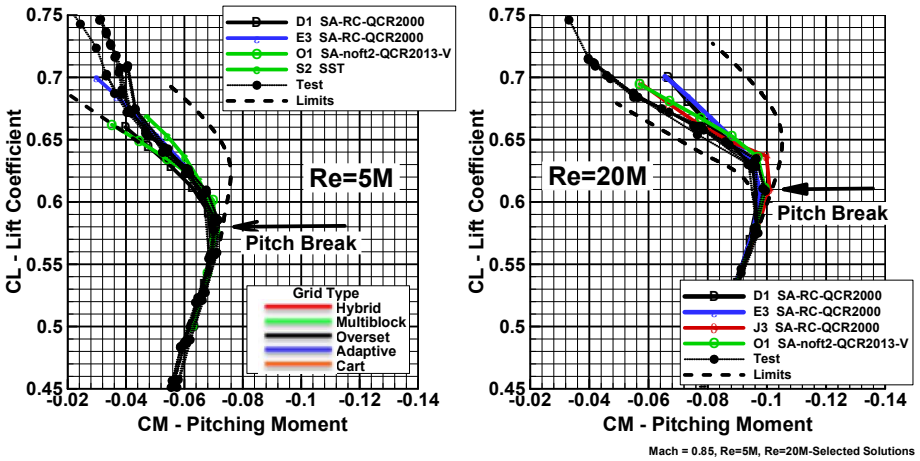

Fig. 40. Selected Lift and Pitching Moment Solutions that Best Match Experiment, Chord Re=20 and 5 million.

For the Case 2b (Chord Re=5 million) four out of 11 solutions matched the experimental data quite well. Three (D1, E3, and O1) used a variation of the SA with QCR turbulence model. The fourth (S2) used some version of the SST turbulence that was not further identified. In terms of grid type three (D1, O1, S2) used a structured multiblock or Overset grid. The other (E3) used an adapted unstructured hybrid type grid. Results from shifted solutions D1, E3, and O1 best matched the experimental force and moment data for both Chord Re=20 million and 5 million. It should be noted in results from DPW-VI for the same case, four of the solutions best matched the experimental data used Overset grids and used a variation of the SA with QCR turbulence model. The other DPW-VI solution used the EARSM turbulence model and an unstructured grid.

Further investigation looked at the wing pressure distributions. Fig. 41 shows pressure distributions at six spanwise locations for an angle-of-attack = 4.25° compared to test data. The wide variation of the shock location on the outboard part of the wing easily explains the scatter of lift and pitching seen in Fig. 38. The four selected solutions that best matched the Chord Re=20 million lift and pitching moment data are shown highlighted in bold red lines. The selected solutions tended to have the most forward shock locations coalescing into two groups, J3 and O1 the most forward shock, followed by D1 and E3. As previously noted, solutions D1 and E3 were starting to deviate from the test data around this condition. Fig. 42 shows the spanwise distribution of sectional lift and pitching moment for an angle-of-attack = 4.25° for all the solutions that were able to generate these data. The selected solutions that best matched the Chord Re=20 million sectional lift and pitching moment data are shown highlighted in bold red lines. Solution O1 had best matched to the test data. J3 did not submit. Pressure distribution and sectional data comparisons for the Case 2b, Chord Re=5 million solutions are quite similar.

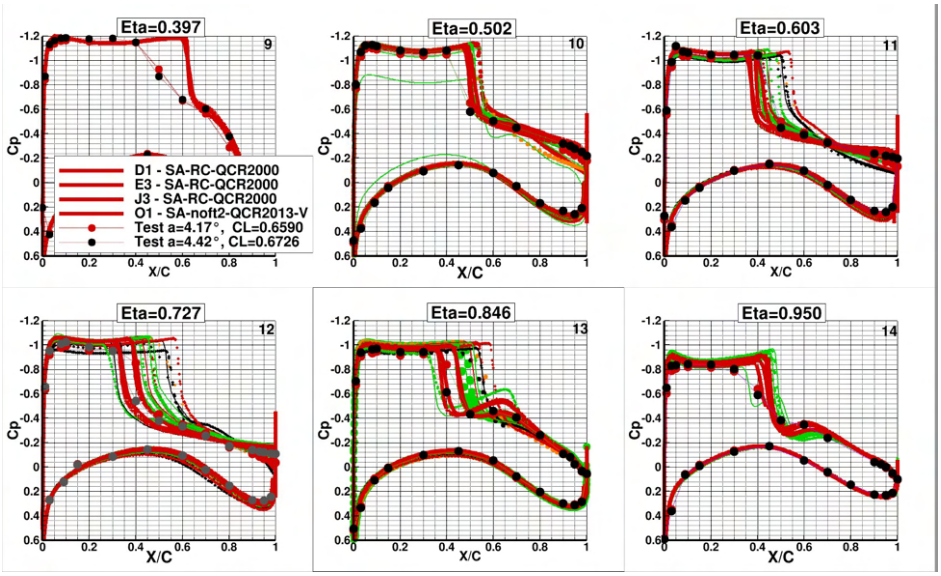

Fig. 41. Pressure Distributions, M=0.85, □=4.25°, Re=20 million– All Solutions (SELECTED SOLUTIONS SHOWN IN RED).

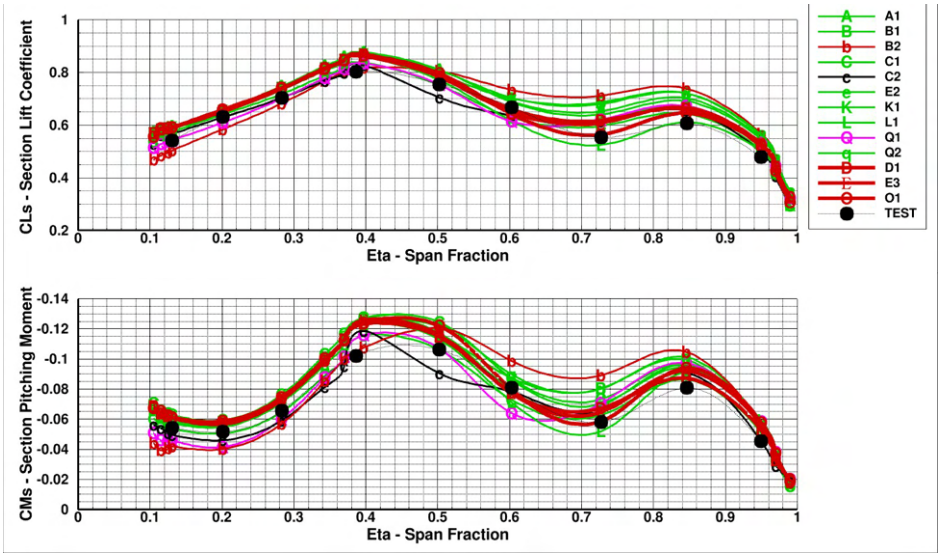

Fig. 42. Wing Spanwise Sectional Lift and Pitching Moment, M=0.85, □=4.25°, Re=20 million All Solutions (SELECTED SOLUTIONS SHOWN IN RED).

While these selected solutions best matched the test data in terms of forces, moments, and pressure distributions one must ask why other solutions using different solvers but essentially the same grids and turbulence models did not. Subtle differences between solver, grid, and turbulence model seem to make large differences in shock-induced separation and the resulting forces and moments.

VII. Observations and Concluding Remarks

The Seventh Drag Prediction Workshop – "Expanding the Envelope" was held in conjunction with AIAA Aviation 2022 conference in Chicago, Il. The event was well attended by a diverse group of expert CFD practitioners from three continents representing government, industry, academia, and commercial code development institutions. 18 teams contributed results. This workshop focused on several studies of the NASA Common Research Model, High Speed CRM wing-body configuration. These included single point

grid convergence and drag increment, high angle-of-attack static buffet conditions, optional grid adaptation, optional "Beyond RANS" and optional coupled aerostructural studies. This paper covers the key results from the workshop.

A primary focus of this workshop was on predicting the effect of shock-induced separation on the variation of lift and pitching moment with increasing angle-of-attack at transonic conditions. Flow conditions dominated by shock-induced separation represent a significant portion of the flight regime critical to safety and government certification regulations. All too often, anomalies in this flight regime are not discovered until flight test resulting in expensive and time-consuming campaigns to "fix" the issue. With sufficient accuracy, reliability, and robustness CFD may help avoid these surprises. The variation of pitching moment with angle-of-attack is a most sensitive indicator in that not only must the lift be adequately predicted but also its distribution along the span of the wing with increasing flow separation. This is a sensitive demonstration of CFD accuracy in predicting this critical behavior. As was done in DPW-VI is the inclusion of the static aeroelastic deformation in the definition of the CRM models for each angle-of-attack/C_L condition specified in the test cases. The inclusion of wing aeroelastic deformation at transonic conditions is essential for accurate CFD predictions. These deformations can be based on measurements taken during a test or on coupled aero-structural simulations.

A total of 34 datasets for the CRM cases were provided on structured, overset, and unstructured grids. One team provided solutions using the same solver and turbulence model but with different grids. Many provided solutions using the same solver and grid but with different turbulence models.

The Case 1 Wing-Body grid convergence study showed similar results to those in DPW-VI but for a higher lift coefficient with stronger shocks. This higher lift coefficient was chosen to challenge the codes at a condition close to the start of the pitching moment break characteristic of the development of significant shock-induced separation. The solutions exhibited a "tighter" convergence of total drag to the continuum with a spread of less than 10 drag counts. Considering that this was a more challenging condition than specified in DPW-VI results here indicate increased robustness in CFD since 2016.

Predicting the effect of shock-induced separation on the variation of lift and pitching moment with increasing angle-of-attack at transonic conditions was addressed by Cases 2, and 4, and to some extent 5 and 6. Case 5 results were limited and not considered adequate for this evaluation. As angle-of-attack is increased the number of outliers observed to have uncharacteristically large wing trailing edge separation at the side-of-body was greatly reduced compared to that seen in DPW-VI. Solutions identifying as only SA and SST turbulence models were most susceptible to the premature side-of-body separation. Experience has shown that premature separation with these turbulence models is very sensitive to gridding details in the wing-body junction region. The use of the quadratic constitutive relation (QCR) in the SA or SST turbulence model is shown to eliminate the premature separation. In addition, solutions using the two-equation turbulence models did not show any evidence of premature side-of-body separation up to at least 4° angle-of-attack (Section VI-A).

All the solutions indicate a higher lift at a given angle-of-attack, and a more negative (nose down) pitching moment at a given lift coefficient than observed in the test data. The primary cause appears to be due the excessive "aft loading" predicted by all the submittals (Section VI-B). This excessive "aft loading" has been seen on other wind tunnel models with significant aft wing camber and deserves further study.

For Cases 2, 4, and 6, the lift and pitching moment results are clustered within a "fan" that gets progressively wider with increasing angle-of-attack. Each one of the solutions on its own is considered a valid solution, yet as angle-of-attack increases so does the spread of shock location on the outboard portion of the wing. Collapsing the computational results to match test data at an attached lift condition allows an assessment of the development of shock-induced separation and its effect on lift and pitching moment as angle-of-attack is increased (Section VI-C). Only 4 of the 34 solutions submitted for the Re=20 million condition closely matched test data. Three of the same (solver, grid type, turbulence model) also closely matched test data for Re=5 million.

New to DPW-VII Case 3 involved calculating a Reynolds number spread from Chord Re=5 million to 30 million at a constant lift coefficient representative of cruise flight. The computation increments were consistent and of the same order as the wind tunnel test increments. There is little difference in choice of turbulence model at this benign flight condition. This will not be the case at more extreme conditions with significant flow separation.

Case 4 requested grid adaptation solutions of the CRM Wing-Body configuration as an optional case. This is an active area of CFD research, and it was time to take another measure of the progress. Four solution

sets were provided by two organizations. Three of the solutions exhibited a strong convergence to the same drag level in the continuum as the fixed grid solutions. The wing pressure distributions from these solutions are essentially indistinguishable from those of the carefully crafted fixed grid solutions but with the characteristic of a sharper definition of the shocks. The promise that solution adaptive grids bring is that they should be able to deliver a consistent set of solutions for configurations, and/or conditions for which prior gridding experience may not be available. Additional work remains to be done to bring this technology to a "production" capability for 3-D RANS. It is a technology that needs to be matured.

Case 5 requested solution technologies beyond steady RANS such as URANS, DDES, WMLES, Lattice Boltzmann, and other scale-resolving schemes. As only two participants submitted data to the workshop, no significant conclusions could be made from the limited data presented. However, discussions regarding the DDES shielding function, which controls the portion of the flowfield computed by the two schemes, followed. Defaults for these shielding parameters, 8 for SA and 15 for Kw-SST Menter models, were recommended. The effect of these values in transonic flowfields should be further investigated. Numerous participants investigated this case and presented results (not yet available for the workshop in 2022) at the AIAA 2023 SciTech Special Session [105,106].

Case 6 requested coupled aero-structural simulations for the second time during the DPW series. The effects of static aeroelastic twist and bending can be very significant at transonic flow conditions. The inclusion of static aeroelastic deformation of the CRM wind tunnel model in the previous DPW-VI attests to their importance. Only two teams submitted solutions in DPW-VII, which prohibits general conclusions from the results. However, a generally good agreement was found between the teams. Participants data show some differences in wing bending deformation, but a good agreement for twist. Accordingly, the resulting wing pressure distributions show a very good agreement over the entire wing, for all angles-of-attack, and were essentially identical to those from the other test cases.

Important issues were raised in this and in previous workshops that point to the need for continuing CFD and experimental research. Previous studies of the influence of the mounting system on the wind tunnel model focused only on the Wing-Body-Tail model. A new CFD study of the CRM wind tunnel mounting system effects is needed. This study should include the effects on the CRM Wing-Body, Wing-Body-Tail, and Wing-Body-Nacelle-Pylon configurations. Excessive "aft loading" was seen from every turbulence model, gridding scheme, and solver type presented in this workshop. It is highly unlikely that this excessive "aft loading" (also seen on other wind tunnel models with significant aft wing camber) is due to experimental issues and more likely a turbulence modeling issue that needs further attention. The wide spread of lift and pitching moment in the CFD solutions at the high angles-of-attack is driven by the predicted shock-induced separation and resulting shock location. The shock location variation at these high angles-of-attack may be physical as well as computational. At 4°, the wind tunnel model experiences a significant amount of buffet. The wind tunnel forces, moments, and pressure data typically represent "average" steady results, but how steady is the flow at these conditions? Is the shock location across the wing steady or moving back and forth? On the CFD side, one must ask if steady Reynolds-Averaged Navier-Stokes (RANS) is adequate for modeling this flow regime in case that unsteady phenomena potentially occur. If the shock movement is small (less than a few percent chord) then RANS is probably adequate. If so, what was it of the four out of 34 solutions that matched the force and pressure data better than the other solutions, many of which used the same grids and turbulence models? These are CFD details that are not well understood. If unsteady shock movement is greater than a few percent chord, will URANS (Unsteady Reynolds Averaged Navier-Stokes) be adequate, or must one go to an eddy-resolving method such as DES (Detached Eddy Simulation) to accurately simulate this flow regime? Additional detailed wind tunnel data, if not already available, is needed to help quantify this issue and to support an improvement of turbulence models, potentially needs for data reinforced models. The magnitude of the unsteady shock movement on the CRM wind tunnel model could be resolved by use unsteady pressure sensitive paint (uPSP) [107]. Answers are necessary to rely on CFD for "Expanding the Envelope."

It is obvious from this and prior workshops that there is an interaction between solver, grid, and turbulence model that becomes most prevalent when there is significant shock-induced separation that we don't understand. These solution sets and experimental data represent a gold mine of information to further the knowledge of CFD and aerodynamics – a great source for graduate student projects. A more detailed report encompassing past DPW-IV, DPW-V, and DPW-VI workshops can be found in Ref. 108.

Acknowledgments

We would like to thank Tecplot for their support throughout the Drag Prediction Workshop Series, as well to other similar CFD workshops.

References

1. 1st AIAA CFD Drag Prediction Workshop, Anaheim, CA, June 2001, http://aiaa-dpw.larc.nasa.gov/Workshop1/workshop1.html, accessed 21 February 2023.
2. Redeker, G., "DLR-F4 Wing-Body Configuration," *A Selection of Experimental Test Cases for the Validation of CFD Codes*, number AR-303, pages B4.1–B4.21. AGARD, August 1994.
3. Levy, D. W., Vassberg, J. C., Wahls, R. A., Zickuhr, T., Agrawal, S., Pirzadeh, S., and Hemsch, M. J., "Summary of data from the first AIAA CFD Drag Prediction Workshop," *Journal of Aircraft*, 40(5) pp. 875–882, Sep–Oct 2003.
4. Hemsch, M. J., "Statistical Analysis of CFD Solutions from the Drag Prediction Workshop," *AIAA Journal of Aircraft,* 41(1) pp. 95-103, 2004.
5. Rakowitz, M., Eisfeld, B., Schwamborn, D., and Sutcliffe, M., "Structured and Unstructured Computations on the DLR-F4 Wing-Body Configuration," *Journal of Aircraft*, 40(2) pp. 256–264, 2003.
6. Mavriplis, D. J. and Levy, D. W., "Transonic Drag Predictions Using an Unstructured Multigrid Solver," *AIAA Journal of Aircraft*, 42(4) pp. 887–893, 2005.
7. Pirzadeh, S. Z. and Frink, N. T., "Assessment of the Unstructured Grid Software TetrUSS for Drag Prediction of the DLR-F4 Configuration," AIAA Paper 2002-0839, 40th AIAA Aerospace Sciences Meeting & Exhibit, Reno, NV, January 2002.
8. Vassberg, J. C., Buning, P. G., and Rumsey, C. L., "Drag Prediction for the DLR-F4 Wing/Body Using OVERFLOW and CFL3D on an Overset Mesh," AIAA Paper 2002-0840, 40th AIAA Aerospace Sciences Meeting & Exhibit, Reno, NV, January 2002.
9. 2nd AIAA CFD Drag Prediction Workshop, Orlando, FL, June 2003, http pp. //aiaa-dpw.larc.nasa.gov/Workshop2/workshop2.html, accessed 21 February 2023.
10. Laflin, K. R., Vassberg, J. C., Wahls, R. A., Morrison, J. H., Brodersen, O., Rakowitz, M., Tinoco, E. N., and Godard, J., "Summary of Data from the Second AIAA CFD Drag Prediction Workshop," *Journal of Aircraft*, 42(5) pp. 1165–1178, 2005.
11. Hemsch, M. and Morrison, J., "Statistical analysis of CFD solutions from 2nd Drag Prediction Workshop," AIAA Paper 2004-0556, 42nd AIAA Aerospace Sciences Meeting and Exhibit, Reno, NV, January 2004.
12. Pfeiffer, N., "Reflections on the Second Drag Prediction Workshop," AIAA Paper 2004-0557, 42nd AIAA Aerospace Sciences Meeting and Exhibit, Reno, NV, January 2004.
13. Brodersen, O. P., Rakowitz, M., Amant, S., Larrieu, P., Destarac, D., and Suttcliffe, M., "Airbus, ONERA and DLR Results from the Second AIAA Drag Prediction Workshop," *Journal of Aircraft*, 42(4) pp. 932–940, 2005.
14. Langtry, R. B., Kuntz, M., and Menter, F., "Drag Prediction of Engine-Airframe Interference Effects with CFX-5," *Journal of Aircraft*, 42(6) pp. 1523–1529, 2005.
15. Sclafani, J., DeHaan, M. A., and Vassberg, J. C., "OVERFLOW Drag Predictions for the DLR-F6 Transport Configuration: A DPW-II Case study," AIAA Paper 2004-0393, 42nd AIAA Aerospace Sciences Meeting and Exhibit, Reno, NV, January 2004.
16. Rumsey, C., Rivers, M., and Morrison, J., "Study of CFD Variations on Transport Configurations from the 2nd AIAA Drag Prediction Workshop," AIAA Paper 2004-0394, 42nd AIAA Aerospace Sciences Meeting and Exhibit, Reno, NV, January 2004.
17. Wutzler, K., "Aircraft Drag Prediction using Cobalt," AIAA Paper 2004-0395, 42nd AIAA Aerospace Sciences Meeting and Exhibit, Reno, NV, January 2004.
18. May, G., Van der Weide, E., Jameson, A., and Shankaran, S., "Drag Prediction of the DLR-F6 Configuration," AIAA Paper 2004-0396, 42nd AIAA Aerospace Sciences Meeting and Exhibit, Reno, NV, January 2004.
19. Kim, Y., Park, S., and Kwon, J., "Drag Prediction of DLR-F6 Using the Turbulent Navier-Stokes Calculations with Multigrid," AIAA Paper 2004-0397, 42nd AIAA Aerospace Sciences Meeting and Exhibit, Reno, NV, January 2004.
20. Yamamoto, K., Ochi, A., Shima, E., and Takaki, R., "CFD Sensitivity to Drag prediction on DLR-F6 Configuration by Structured Method and Unstructured Method," AIAA Paper 2004-0398, 42nd AIAA Aerospace Sciences Meeting and Exhibit, Reno, NV, January 2004.
21. Tinoco, E. and Su, T., "Drag Prediction with the Zeus/CFL3D System," AIAA Paper 2004-0552, 42nd AIAA Aerospace Sciences Meeting and Exhibit, Reno, NV, January 2004.
22. 3rd AIAA CFD Drag Prediction Workshop, San Francisco, CA, June 2006, http://aiaa-dpw.larc.nasa.gov/Workshop3/workshop3.html, accessed 21 February 2023.
23. Vassberg, J. C., Sclafani, A. J., and DeHaan, M. A., "A Wing-Body Fairing Design for the DLR-F6 Model: A DPW-III Case Study," AIAA Paper 2005-4730, AIAA 23rd Applied Aerodynamics Conference, Toronto, Canada, June 2005.

24. Vassberg, J. C., Tinoco, E. N., Mani, M., Brodersen, O. P., Eisfeld, B., Wahls, R. A., Morrison, J. H., Zickuhr, T., Laflin, K. R., and Mavriplis, D. J., "Abridged Summary of the Third AIAA CFD Drag Prediction Workshop," *Journal of Aircraft*, 45(3) pp. 781–798, May–June 2008.
25. Vassberg, J. C., Tinoco, E. N., Mani, M., Brodersen, O. P., Eisfeld, B., Wahls, R. A., Morrison, J. H., Zickuhr, T., Laflin, K. R., and Mavriplis, D. J., "Summary of DLR-F6 Wing-Body Data from the Third AIAA CFD Drag Prediction Workshop," RTO AVT-147 Paper 57, RTO AVT-147 Symposium, Athens, Greece, December 2007.
26. Morrison, J. H. and Hemsch, M. J., "Statistical Analysis of CFD Solutions from the Third AIAA Drag Prediction Workshop," AIAA Paper 2007-0254, 45th AIAA Aerospace Sciences Meeting and Exhibit, Reno, NV, January 2007.
27. Tinoco, E. N., Winkler, C., Mani, M., and Venkatakrishnan, V., "Structured and Unstructured Solvers for the 3rd CFD Drag Prediction Workshop," AIAA Paper 2007-0255, 45th AIAA Aerospace Sciences Meeting and Exhibit, Reno, NV, January 2007.
28. Mavriplis, D. J., "Results from the 3rd Drag Prediction Workshop Using the NSU3D Unstructured Mesh Solver," AIAA Paper 2007-0256, 45th AIAA Aerospace Sciences Meeting and Exhibit, Reno, NV, January 2007.
29. Sclafani, A. J., Vassberg, J. C., Harrison, N. A., DeHaan, M. A., Rumsey, C. L., Rivers, S. M., and Morrison, J. H., "Drag Predictions for the DLR-F6 Wing/Body and DPW Wings Using CFL3D and OVERFLOW on an Overset Mesh," AIAA Paper 2007-0257, 45th AIAA Aerospace Sciences Meeting and Exhibit, Reno, NV, January 2007.
30. Brodersen, O., Eisfeld, B., Raddatz, J., and Frohnapfel, P., "DLR Results from the Third AIAA CFD Drag Prediction Workshop," AIAA Paper 2007-0259, 45th AIAA Aerospace Sciences Meeting and Exhibit, Reno, NV, January 2007.
31. Tinoco, E. N., Venkatakrishnan, V., Winkler, C., and Mani M., "Structured and Unstructured Solvers for the Third AIAA CFD Drag Prediction Workshop," *Journal of Aircraft*, 45(3) pp. 738–749, May–June 2008.
32. Mavriplis, D. J., "Third Drag Prediction Workshop Results Using NSU3D Unstructured Mesh Solver," *Journal of Aircraft*, 45(3) pp. 750–761, May–June 2008.
33. Sclafani, A. J., Vassberg, J. C., Harrison, N. A., Rumsey, C. L., Rivers, S. M., and Morrison, J. H., "CFL3D / OVERFLOW Results for DLR-F6 Wing/Body and Drag Prediction Workshop Wing," *Journal of Aircraft*, 45(3) pp. 762–780, May–June 2008.
34. Murayama, M. and Yamamoto, K., "Comparison Study of Drag Prediction by Structured and Unstructured Mesh Method," *Journal of Aircraft*, 45(3) pp. 799–822, May–June 2008.
35. Brodersen, O., Eisfeld, B., Raddatz, J., and Frohnapfel, P., "DLR results from the third AIAA Computational Fluid Dynamics Drag Prediction Workshop," *Journal of Aircraft*, 45(3) pp. 823–836, May–June 2008.
36. Eliasson, P. and Peng, S.-H., "Drag Prediction for the DLR-F6 Wing-Body Configuration Using the Edge Solver," *Journal of Aircraft*, 45(3) pp. 837–847, May–June 2008.
37. Mavriplis, D. J., Vassberg, J. C., Tinoco, E. N., Mani, M., Brodersen, O. P., Eisfeld, B., Wahls, R. H., Morrison, J., Zickuhr, T., Levy, D., and Murayama, M., "Grid quality and Resolution Issues from the Drag Prediction Workshop Series," *Journal of Aircraft*, 46(3) pp. 935–950, 2009.
38. 4thAIAA CFD Drag Prediction Workshop, San Antonio, TX, June 2009, http://aiaa-dpw.larc.nasa.gov/Workshop4/workshop4.html, accessed 21 February 2023.
39. Vassberg, J. C., DeHaan, M. A., Rivers, S. M., and Wahls, R. A., "Development of a Common Research Model for Applied CFD Validation Studies," AIAA Paper 2008-6919, 26th AIAA Applied Aerodynamics Conference, Hawaii, HI, August 2008, *and Journal of Aircraft*, 55(4) pp. 1325-1337, 2018.
40. Vassberg, J., Tinoco, E., Mani, M., Rider, B., Zickuhr, T., Levy, D., Broderson, O., Eisfeld, B., Crippa, S., Wahls, R., Morrison, J., Mavriplis, D., Murayama, M., "Summary of the Fourth AIAA CFD Drag Prediction Workshop," AIAA 2010-4547, 28th AIAA Applied Aerodynamics Conference, Chicago, IL, June 2010.
41. Morrison, J., "Statistical Analysis of CFD Solutions from the Fourth Drag Prediction Workshop," *Journal of Aircraft*, 2014, 51(4), 1070-1089.
42. Sclafani, A. J., Vassberg, J. C., Rumsey, C., DeHaan, M. A., and Pulliam, T. H., "Drag Prediction for the NASA CRM Wing/Body/Tail Using CFL3D and OVERFLOW on an Overset Mesh," *Journal of Aircraft*, 2014, 51(4), 1101-1117.
43. Hue, D., Gazaix, M., and Esquieu, S., "Computational Drag and Moment Prediction of the DPW4 Configuration with elsA," AIAA Paper 2010-4220, 28th AIAA Applied Aerodynamics Conference, Chicago, IL, June 2010.
44. Mani, M., Rider, B. J., Sclafani, A. J., Winkler, C., Vassberg, J. C., Dorgan, A. J., Cary, A., and Tinoco, E. N., "RANS Technology for Transonic Drag Prediction; a Boeing Perspective of the 4th Drag Prediction Workshop," *Journal of Aircraft*, 2014, 51(4), 1118-1134.
45. Yamamoto, K., Tanaka, K., and Murayama, M., "Comparison Study of Drag Prediction for the 4th CFD Drag Prediction Workshop Using Structured and Unstructured Mesh Methods," AIAA Paper 2010-4222, 28th AIAA Applied Aerodynamics Conference, Chicago, IL, June 2010.
46. Brodersen, O., Crippa, S., Eisfeld, B., Keye, S., and Geisbauer, S., "DLR Results for the Fourth AIAA CFD Drag Prediction Workshop," *Journal of Aircraft,* 2014, 51(4), 1135-1148.

47. Eliasson, P., Peng, S., and Tysell, L., "Computations from the 4th Drag Prediction Workshop Using the Edge Solver," AIAA Paper 2010-4548, 28th AIAA Applied Aerodynamics Conference, Chicago, IL, June 2010.
48. Li, G. and Zhou, Z., "Validation of a Multigrid-Based Navier-Stokes Solver for Transonic Flows," AIAA Paper 2010-4549, 28th AIAA Applied Aerodynamics Conference, Chicago, IL, June 2010.
49. Mavriplis, D. J. and Long, M., "NSU3D Results for the Fourth AIAA Drag Prediction Workshop," *Journal of Aircraft*, 2014, 51(4), 1161-1171.
50. Lee-Rausch, E., Hammond, E., Nielsen, E., Pirzadeh, S., and Rumsey C., "Application of the FUN3D Unstructured-Grid Navier-Stokes Solver to the 4th AIAA Drag Prediction Workshop Cases," *Journal of Aircraft*, 2014, 51(4), 1149-1160.
51. Vos, J., Sanchi, S., Gehri, A., and Stephani, P., "DPW4 Results Using Different Grids, Including Near-Field/Far-Field Drag Analysis," AIAA Paper 2010-4552, 28th AIAA Applied Aerodynamics Conference, Chicago, IL, June 2010.
52. Hashimoto, A., Lahur, P., Murakami, K., and Aoyama, T., "Validation of Fully Automatic Grid Generation Method on Aircraft Drag Prediction," AIAA Paper 2010-4669, 28th AIAA Applied Aerodynamics Conference, Chicago, IL, June 2010.
53. Hashimoto, Atsushi, Keiichi Murakami, Takashi Aoyama, Kazuomi Yamamoto, Mitsuhiro Murayama, and Paulus R. Lahur, "Drag Prediction on NASA Common Research Model Using Automatic Hexahedra Grid-Generation Method," *Journal of Aircraft*, 2014, 51(4) pp. 1172-1182
54. Temmerman, L. and Hirsch, C., "Simulations of the CRM Configuration on Unstructured Hexahedral Grids: Lessons Learned from the DPW-4 Workshop," AIAA Paper 2010-4670, 28th AIAA Applied Aerodynamics Conference, Chicago, IL, June 2010.
55. Chaffin, M. and Levy, D., "Comparison of Viscous Grid Layer Growth Rate of Unstructured Grids on CFD Drag Prediction Workshop Results," AIAA Paper 2010-4671, 28th AIAA Applied Aerodynamics Conference, Chicago, IL, June 2010.
56. Crippa, S., "Application of Novel Hybrid Mesh Generation Methodologies for Improved Unstructured CFD Simulations," AIAA Paper 2010-4672, 28th AIAA Applied Aerodynamics Conference, Chicago, IL, June 2010.
57. 5th AIAA CFD Drag Prediction Workshop, http://aiaa-dpw.larc.nasa.gov/Workshop5/workshop5.html, accessed 21 February 2023.
58. Vassberg, J. C., "A Unified Baseline Grid about the Common Research Model Wing-Body for the Fifth AIAA CFD Drag Prediction Workshop," AIAA Paper 2011-3508, 29th AIAA Applied Aerodynamics Conference, Honolulu, HI, June 2011.
59. Rumsey, C., "Langley Research Center Turbulence Modeling Resource," http://turbmodels.larc.nasa.gov/, accessed 21 February 2023.
60. Levy, D. W., Laflin, K. R., Tinoco, E. N., Vassberg, J. C., Mani, M., Rider, B., Rumsey, C. L., Wahls, R. A., Morrison, J. H., Brodersen, O. P., Crippa, S., Mavriplis, D. J., and Murayama, M., "Summary of Data from the Fifth Computational Fluid Dynamics Drag Prediction Workshop," *Journal of Aircraft*, 2014, 51(4) pp. 1194-1213
61. Morrison, J. H., "Statistical Analysis of the Fifth Drag Prediction Workshop Computational Fluid Dynamics Solutions," *Journal of Aircraft,* 2014, 51(4) pp. 1214-1222.
62. Sclafani, A. J., Vassberg, J. C., Winkler, C., Dorgan, A. J., Mani, M., Olsen, M. E., and Coder, J. G., "Analysis of the Common Research Model Using Structured and Unstructured Meshes," *Journal of Aircraft,* 2014, 51(4) pp. 1223-1243
63. Murayama, M., Yamamoto, K., Hashimoto, A., Ishida, T., Ueno, M., Tanaka, K., and Ito, Y., "Japan Aerospace Exploration Agency Studies for the Fifth AIAA Drag Prediction Workshop," *Journal of Aircraft,* 2014, 51(4) pp. 1244-1267
64. Park, M. A., Laflin, K. R., Chaffin, M. S., Powell, N., and Levy, D. W., "CFL3D, FUN3D, and NSU3D Contributions to the Fifth Drag Prediction Workshop," *Journal of Aircraft,* 2014, 51(4) pp. 1268-1283
65. Ceze, M. and Fidkowski, K. J., "Drag Prediction Using Adaptive Discontinuous Finite Elements," *Journal of Aircraft,* 2014, 51(4), 1284-1294
66. Hue, D., "Fifth Drag Prediction Workshop: Computational Fluid Dynamics Studies Carried Out at ONERA," *Journal of Aircraft,* 2014, 51(4), 1295-1310
67. Hue, D., "Fifth Drag Prediction Workshop: ONERA Investigations with Experimental Wing Twist and Laminarity," *Journal of Aircraft,* 2014 51(4), 1311-1322
68. Keye, S., Brodersen, O., and Rivers, M. B., "Investigation of Aeroelastic Effects on the NASA Common Research Model," *Journal of Aircraft,* 2014, 51(4), 1323-1330
69. Eberhardt, S., Benedict, K., Hedges, L., Robinson, A., and Tinoco, E. N., "Inclusion of Aeroelastic Twist into the CFD Analysis of the Twin-Engine NASA Common Research Model," AIAA Paper 2014-0251, 52nd AIAA Aerospace Sciences Meeting, National Harbor, MD, January 2014.
70. Togiti, V., Eisfeld, B., and Brodersen, O., "Turbulence Model Study for the Flow Around the NASA Common Research Model," *Journal of Aircraft,* 2014, 51(4), 1331-1343
71. Special Section: Drag Prediction Workshops IV and V, *Journal of Aircraft*, 51(4), pp. 1069–1069, 2014.

72. 6th AIAA CFD Drag Prediction Workshop, Washington DC, June 2016, https://aiaa-dpw.larc.nasa.gov/Workshop6/workshop6.html, accessed 21 February 2023.
73. Roy, C. J., Rumsey, C., and Tinoco, E. N., "Summary of Data from the Sixth AIAA CFD Drag Prediction Workshop: Case 1 Code Verification," *Journal of Aircraft*, 55(4), pp. 1338-1351, 2018.
74. Tinoco, Edward N., Brodersen, Olaf P., Keye, Stefan, Laflin, Kelly R., Feltrop, Edward, Wahls, Richard A., Morrison, Joseph H., Vassberg, John C., Mani, Mori, Rider, Ben, Hue, David, Roy, Christopher J., Mavriplis, Dimitri J., and Murayama, Mitsuhiro, "Summary of Data from the Sixth AIAA CFD Drag Prediction Workshop: CRM Cases 2 to 5" *Journal of Aircraft*, 55(4), pp. 1352-1379, 2018.
75. Derlaga, J. M. and Morrison, J. H., "Statistical Analysis of CFD Solutions from the Sixth AIAA Drag Prediction Workshop," *Journal of Aircraft*, 55(4), pp. 1388-1400, 2018.
76. Keye, S. and Mavriplis, D., "Summary of Case 5 from Sixth Drag Prediction Workshop: Coupled Aerostructural Simulation," *Journal of Aircraft*, 55(4), pp. 1380-1387, 2018.
77. Coder, J.G., Hue, D., Kenway, G., Pulliam, T. H., Sclafani, A.J., Serrano, L., Vassburg, J.C., "Contributions to the Sixth Drag Prediction Workshop Using Structured, Overset Grid Methods," *Journal of Aircraft*, 55(4), pp.1406-1419, 2018.
78. Michal, T., Babcock, D., Kamenetsky, D., Krakos, J., Mani, M., Glasby, FR., Erwin, T., Stefanski, D.L. "Comparison of Fixed and Adaptive Unstructured Grid Results for Drag Prediction Workshop 6," *Journal of Aircraft*, 55(4), pp.1420-1432, 2018.
79. Ito, Y., Murayama, H., Hashimoto, A., Ishida, T., Yamamoto, K., Aoyama, T., Tanaka, K., Hayashi, K., Ueshima, K., Nagata, T., Ueno, Y., Ochi, A., "TAS Code, FaSTAR, and Cflow Results for the Sixth drag Prediction Workshop," *Journal of Aircraft*, 55(4), pp. 1433-1457. 2018.
80. Abdoi-Hamid, K.S., Carlson, J.R., Rumsey, C.L., Lee-Rausch, F.M., Park, M.A., "Sixth Drag Prediction Workshop Results Using FUN3D with k-ki-MEAH2015 Turbulence Model," *Journal of Aircraft*, 55(4), pp.1456-1468, 2018.
81. Chen, J., Zhang, Y., Zhao, H., Zhou, G., "Numerical Investigations of the NASA Common Research Model with Aeroelastic Twist," *Journal of Aircraft*, 55(4), pp. 1469-1481, 2018.
82. Konig, B., Fares, E., "Exa PowereFLOW Simulations for the Sixth AIAA Drag Prediction Workshop," *Journal of Aircraft*, 55(4), pp. 1482-1490, 2018.
83. Cartieri A., Hue D., and Chanzy Q, "Experimental Investigations on Common Research Model at ONERA-S1MA–Drag Prediction Workshop Numerical Results", *Journal of Aircraft*, 55(4), pp. 1491-1508, 2018.
84. Hue, D., Chanzy, Q., Landier, O., "DPW-6 Drag Analyses and Increments Using different Geometries of the Common Research Model Airliner," *Journal of Aircraft*, 55(4), pp. 1509-1521, 2018.
85. "Introduction to Special Section – DPW-VI," *Journal of Aircraft*, 55(4), pp.1317-1324, 2018.
86. 7th AIAA CFD Drag Prediction Workshop, Chicago, IL, June 2022, http://aiaa-dpw.larc.nasa.gov, accessed 21 February 2023.
87. Tinoco, E.N., "Analysis of the Transonic NASA Common Research Model at High Angle of Attack," AIAA-2020-2745, 2020 AIAA AVIATION Forum and Exposition, June 2020
88. Rivers, M. and Dittberner, A., "Experimental Investigations of the NASA Common Research Model," AIAA Paper 2010-4218, 28th AIAA Applied Aerodynamics Conference, Chicago, IL, June 2010.
89. Rivers, M. and Dittberner, A., "Experimental Investigations of the NASA Common Research Model in the NASA Langley National Transonic Facility and NASA Ames 11-Ft Transonic Wind Tunnel (Invited)," AIAA Paper 2011-1126, presented at the 49th Aerospace Sciences Meeting, Orlando, FL, Jan 2011.
90. Common Research Model, http://commonresearchmodel.larc.nasa.gov/, accessed 21 February 2023.
91. European Transonic Wind Tunnel: ETW, https://www.etw.de /, accessed 21 February 2023.
92. ETW CRM wind tunnel test data, https://commonresearchmodel.larc.nasa.gov/european-transonic-wind-tunnel-data, accessed 21 February 2023
93. Ueno, M., Kohzai, T., and Koga, S., "Transonic Wind Tunnel Test of the NASA CRM (Volume 1)," JAXA-RM-13-01E, March 2013.
94. Rivers, M. and Hunter, C., "Support System Effects on the NASA Common Research Model," AIAA Paper 2012-707, 50th AIAA Aerospace Sciences Meeting, January 2012.
95. Rivers, M., Hunter, C., and Campbell, R., "Further Investigation of the Support System Effects and Wing Twist on the NASA Common Research Model," AIAA Paper 2012-3209, 30th AIAA Applied Aerodynamics Conference, New Orleans, LA June 2012.
96. Keye, S. and Gammon, M. R., "Development of Deformed CAD Geometries of NASA's Common Research Model for the 6th AIAA CFD Drag Prediction Workshop," *Journal of Aircraft*, 55(4), pp. 1401-1405, 2018.
97. Ito, Y. and Nakahashi, K., "Direct Surface Triangulation Using Stereolithography Data," *AIAA Journal*, Vol. 40, No. 3, March 2002, pp. 490-496, DOI: 10.2514/2.1672.
98. Ito, Y., Murayama, M., Yamamoto, K., Shih, A. M. and Soni, B. K., "Efficient Hybrid Surface/Volume Mesh Generation Using Suppressed Marching Direction Method," *AIAA Journal*, Vol. 51, No. 6, June 2013, pp. 1450-1461, DOI: 10.2514/1. J052125.

99. Martineau, D., Stokes, S., Munday, S., Jackson, A., Gribben, B., and Verhoeven, N., "Anisotropic Hybrid Mesh Generation for Industrial RANS Applications," AIAA Paper 2006-0534, Jan. 2006.
100. Kamenetskiy, Dmitry S., Krakos, Joshua A., Michal, Todd R., Clerici, Francesco, Alauzet, Frederic, Loseille, Adrien, Park, Michael A., Wood, Stephen L., Balan, Aravind, and Galbraith, Marshall C., "Anisotropic Goal-Based Mesh Adaptation Metric Clarification and Development," AIAA Scitech 2022 Forum, January 2022, San Diego CA, https://doi.org/10.2514/6.2022-1245.
101. Michael, T., and Krakos, J., "Anisotropic Mesh Adaptation Through Edge Primitive Operations," AIAA Paper 2012-159, 50th AIAA Aerospace Sciences Meeting, January 2012.
102. Glasby, R. S., Erwin, J. T., Stefanski, D. L., Allmaras, S. R., Galbraith, M. C., Anderson, W. K., and Nichols, R. H., "Introduction to COFFE: The Next-Generation HPCMP CREATETM-AV CFD Solver," AIAA Paper 2016-0567, 54th AIAA Aerospace Sciences Meeting, January 2016.
103. NASA Juncture Flow Experiment, https://turbmodels.larc.nasa.gov/Other_exp_Data/junctureflow_exp.html assessed 22nd January 2023.
104. Kegerise M. A., Neuhart D. H., Hannon J. A. and Rumsey C. L., "An Experimental Investigation of a Wing-Fuselage Junction Model in the NASA Langley 14- by 22-Foot Subsonic Wind Tunnel," AIAA Paper 2019-0077, AIAA Scitech 2019 Forum, January 2019. https://doi.org/10.2514/6.2019-0077
105. Fournis, C., Petropoulos, I., Sartor, F., "Unsteady Far-Field Drag Analyses of Transonic Buffet over the NASA Common Research Model," *(57th 3AF International Conference on Applied Aerodynamics (AERO2023), 29-31 March 2023, Bordeaux, France)*
106. Hue, D., Sartor, F., Petropoulos, I., and Fournis, C., "DPW-7: Steady and Unsteady Computations of the CRM Aircraft at Different Reynolds Numbers Scheme/methodology for Case 5: URANS," *(article draft submitted to the Journal of Aircraft, currently under review)*
107. https://www.nasa.gov/feature/pressure-sensitive-paint-for-measuring-unsteady-launch-vehicle-aerodynamic-buffet , accessed 22 March 2023
108. Tinoco, Edward N., "An Evaluation and Recommendations for Further CFD Research Based on the NASA Common Research Model (CRM) Analysis from the AIAA Drag Prediction Workshop (DPW) Series," NASA/CR-2019-220284, ntrs.nasa.gov, January 2019.